Algorithms for Wind Parameter Retrieval from Rain-contaminated X-band Marine Radar Images

by

© Yali Wang, B. Eng.

A thesis submitted to the School of Graduate Studies

in partial fulfilment of the requirements for the degree of

Master of Engineering

Department of Electrical and Computer Engineering

Faculty of Engineering and Applied Science

Memorial University of Newfoundland

May, 2016

St. John's   Newfoundland

Abstract

In this thesis, research for retrieving wind direction and speed from rain-contaminated X-band marine radar images is presented. Firstly, a method for retrieving wind direction from X-band marine radar data is proposed. The algorithm is used to investigate radar backscatter in the wavenumber domain and obtain wind direction from the wavenumber spectrum. For rain-contaminated images collected under low wind speeds (i.e. less than 8 m/s), wind directions are retrieved using spectral components with wavenumbers of [0.01, 0.2] rad/m. For rain-contaminated images obtained under high wind speeds and rain-free images, wind directions are retrieved using the spectral values at wavenumber zero. The algorithm was tested using X-band radar images and anemometer data collected on the east coast of Canada. Comparison with the anemometer data shows that the root mean square error (RMSE) of wind directions retrieved from low-wind-speed rain-contaminated images is reduced by 25.1°. Secondly, two methods for estimating wind speed from X-band nautical radar images are presented. One method is used to determine wind speeds by relating the spectral strengths of radar backscatter to the wind speeds using a logarithmic function. The other method is used to mitigate rain influence by applying gamma correction to rain-contaminated images, and then relate the average radar image intensities to measured wind speeds with a logarithmic function. Comparison with the anemometer data show that the two methods reduce the RMSEs of wind speeds estimated from rain-contaminated radar data by 5.9 m/s and 5.4 m/s, respectively. Unlike existing methods which require the exclusion of rain-contaminated data, the new wind parameter retrieval methods work well for both rain-contaminated and rain-free images.

Acknowledgements

Contents

List of Tables

List of Figures

List of Symbols

The page numbers here indicate the place of first significant reference. Symbols which are not explicitly referenced below, have definitions which are obvious from the context.

$$
\begin{aligned}
d \quad &: \quad \text{The distance of the reflective sub-surface (p. 3).}\\
\lambda \quad &: \quad \text{The electromagnetic wavelength (p. 3).}\\
\phi \quad &: \quad \text{The incidence angle of electromagnetic wave on sea surface (p. 3).}\\
m \quad &: \quad \text{The order of scattering (p. 3).}\\
\theta \quad &: \quad \text{Azimuth direction angle (p. 11).}\\
\sigma_\theta \quad &: \quad \text{The average image intensity in azimuth direction } \theta \text{ (p. 11).}\\
a_0,\, a_1,\, a_2 \quad &: \quad \text{Regression parameters for least-square fitting (p. 11).}\\
N \quad &: \quad \text{The total number of backscatter samples in one azimuth (p. 12).}\\
n \quad &: \quad \text{The number of backscatter samples in one azimuth (p. 12).}\\
I_\theta(n) \quad &: \quad \text{The } n\text{th pixel intensity in azimuth direction } \theta \text{ (p. 12).}\\
k \quad &: \quad \text{Wavenumber (p. 12).}\\
E_\theta(k) \quad &: \quad \text{The spectral value of wavenumber } k \text{ in azimuth direction } \theta \text{ (p. 12).}\\
E_\theta(0) \quad &: \quad \text{The spectral value of wavenumber } 0 \text{ in azimuth direction } \theta \text{ (p. 12).}
\end{aligned}
$$

$\lvert E_\theta(0)\rvert$	:	The absolute value of $E_\theta(0)$ (p. 12).
S_θ	:	The integral of the normalized spectra over the wavenumber range [0.01, 0.2] rad/m (p. 14).
σ_{ws}	:	The average of σ_θ (p. 31).
w	:	Wind speed (p. 31).
$b_0,\ b_1,\ b_2,\ b_3$	:	Regression parameters for least-square fitting (p. 31).
$S_{nonzero}$	:	The average of the nonzero components in the wavenumber spectra (p. 33).
k_N	:	The Nyquist wavenumber (p. 33).
Δr	:	Range resolution (p. 33).
k_1	:	The first nonzero wavenumber (p. 33).
S_{zero}	:	The average of the zero components in the wavenumber spectra (p. 33).
S	:	The summation of S_{zero} and $S_{nonzero}$ (p. 34).
I_{max}	:	The maximum image intensity of an image (p. 36).
I_{in}	:	The normalized image intensity (p. 36).
I_{out}	:	The gamma corrected image intensity (p. 36).
$i,\ j$	:	The row and column number of a pixel (p. 36).
γ	:	Gamma correction factor (p. 36).
I_{ave}	:	The average intensity of the gamma corrected image (p. 39).

Chapter 1

Introduction

1.1 Research Rationale

Marine radars which are usually installed on ships can detect targets nearby. The equipment works by transmitting electromagnetic waves to the sea surface and collecting the backscattered signal. Typically, the electromagnetic waves transmitted by marine radars are in X-band (8 to 12 GHz) or S-band (2 to 4 GHz). This work focuses on X-band marine radar, whose radio wavelength is about 3 cm. While X-band marine radars were originally used for target detection, they can also be used to collect sea surface information. The interaction between the transmitted electromagnetic waves and sea surface waves leads to the changes in radar backscatter which result in wave patterns in the radar images [1]. The wave patterns appearing in marine radar images have been observed since 1960 [2,3]. However, these patterns were considered as noise and eliminated for ship navigation [4]. In the 1980s, researchers began to investigate marine radar images which contain abundant wave information [5–7]. X-

1

band marine radar was used for various sea surface measurements and became a new tool for ocean remote sensing [8–12].

Compared with traditional remote sensing systems, such as synthetic aperture radar (SAR) and high-frequency (HF) radar, marine radar systems are more cost-effective and flexible for routine measurements [7]. For example, although SAR systems can be used to obtain ocean measurements, they are too expensive for routine measurements of specific ranges, since they need to be installed on aircraft or satellites for remote sensing [11]. Moreover, the time interval for SAR to revisit a specific location is in the order of days, while the measurement interval for marine radar is in the order of seconds [12, 13]. HF radars are typical installed onshore due to the size of the system [14]. Marine radars can be a complement to HF radars, since the they can be installed on a ship to obtain measurements of the open sea.

The sea surface parameters that can be measured using X-band marine radars include sea surface wave height, wind direction and wind speed. Traditionally, wave information was collected by buoys. However, buoys provide only temporal point measurements while marine radar can image sea surface waves both temporally and spatially [15]. Sea state parameters are closely related to wind conditions, since the frictional force of the wind field generates sea surface roughness [16–20]. Wind direction and speed can be estimated by analysing radar images that contain wave patterns. Unlike measurements obtained using traditional wind sensors such as anemometers, the estimated wind information from radar images is less affected by air flow distortion due to the instrument's platform. In this research, wind parameter retrieval from X-band marine radar images is investigated.

2

1.2 Literature Review

Sea surface wind information is important for marine navigation. Such information may be obtained from anemometers as well as X-band marine radar images. As noted, the advantage of marine radars is that they are less likely to be affected by the air flow distortion introduced by the ship's pitch and roll. Moreover, the extra cost to obtain wind information from such radars is not significant, since they are already installed on ships [21].

The most important mechanism contributing to the interaction between radar and ocean waves is Bragg scattering [1], which could be writen as [22]

$$d = \frac{m\lambda}{2\sin\phi} \tag{1.1}$$

where d is the distance of the reflective sub-surfaces, λ is the electromagnetic wavelength, ϕ is the incidence angle, m is the order of scattering. For X-band marine radar working at grazing incidence, $\lambda = 3cm$, $\phi \approx 90°$, and the scattering from the first order, i.e. $m = 1$, is considered to be the strongest [1]. Thus, sea surface capillary waves with wavelengths in the cm-scale contribute to X-band radar backscatter [23]. Considering the sea surface as a composition of small capillary waves riding on the top of large gravity waves, in 1968 Wright [24] proposed a composite scattering model. The model effectively explained microwave scattering characteristics at intermediate incidence angles [25–28]. However, measured radar backscatter intensities were always higher than that predicted using Wright's model for HH (horizontal transmit and horizontal receive) -polarized radar operating at large incidence (or low grazing) angles [29]. To explain this phenomenon, Lyzenga *et al.* [30] pointed out that the scattering from wave wedges should be considered. In the 1990s, it was found

3

that the contribution of wave breaking to the radar cross section is significant and may increase with the friction velocity of the wind [31–33]. Although the microwave scattering mechanism at grazing incidence is not yet fully understood, it is well accepted that the modulation of long gravity waves to small surface waves combined with tilt and shadowing effects cause changes in the radar backscatter, resulting in wave patterns in radar images [16, 21, 34–36].

Spectral analyses of radar images were conducted in the 1980s. In 1982, Hoogeboom and Rosenthal [37] obtained two-dimensional power spectra by digitalizing radar backscatter and applying the two-dimensional Fourier transform on the corresponding radar images. It was found that the two-dimensional power spectra obtained from radar images agreed well with those obtained from buoys [38]. However, a 180° directional ambiguity existed in the obtained spectra [6]. In 1985, Atanassov *et al.* [6] proposed a method to remove the directional ambiguity by performing Fourier transform on two sequential images along with an application of the dispersion relationship. In the same year, Young *et al.* [7] performed three-dimensional analysis on radar images which also successfully solved the ambiguity problem. This exhibited the possibility of using the spectral analysis of radar images for retrieving sea surface information. However, these techniques for retrieving wind information were more widely applied to SAR images instead of marine radar images [39, 40].

Methods for retrieving wind information from marine radar images are derived based on the fact that radar backscatter intensity varies with azimuth directions and wind speeds. Two observations aid wind direction retrieval, one of them being that linear features, i.e. wind streaks, are well-aligned with the mean wind direction on the averaged radar images [19]. The other observation is that the radar backscatter

intensity exhibits a single peak in the upwind direction [41,42]. Various wind direction retrieval methods were proposed based on these two observations [20,21,43].

In 2003, Dankert *et al.* [19,20] performed space domain analysis on X-band marine radar images. By averaging marine radar image sequences every 2 minutes, they observed wind-induced streaks and from there determined wind direction from averaged radar images. The directional ambiguity can be removed by calculating the cross-correlation between image sequences. Wind speed is retrieved by relating the normalized radar cross sections (NRCS) to the measured wind speeds using neural networks. The radar-retrieved wind directions and speeds coincide well with anemometer measurements. However, this method is more suitable for wind information retrieval from a fixed platform than from a moving platform, since wind-induced streaks are difficult to be identified from data collected on moving platforms such as ships [21].

In 2012, a method for wind information retrieval from shipborne radar data was proposed by Lund *et al.* [21]. This method is based on the fact that for HH-polarized radar operating at grazing incidence, radar backscatter intensities exhibit a single peak in the upwind direction [41,42]. In [21], after averaging of the radar intensities in each azimuth, a sinusoidal function is used to least-squares fit the averaged intensities according to azimuth directions. The wind direction is determined as the peak of the fitted curve. For wind speed, a third-order polynomial is utilized to relate the average intensity of the whole image to the measured wind speed. This method could be applied to data collected by a fixed or moving platform, and even with partly-shadowed images. Another method for retrieving wind information from shipborne data was proposed in 2013 by Vicen-Bueno *et al.* [43]. In that method, radar images

5

are first integrated and smoothed every 2 minutes. Then, a specific intensity is selected as the intensity threshold. The range distance corresponding to the specific intensity is calculated in each azimuth direction. Wind direction is determined as the direction which has the maximum range distance. Wind speed is retrieved by relating the maximum range distances to the measured wind speeds using a third-order polynomial. Compared with Lund's method, the wind direction and speed retrieved using this method has a slightly higher accuracy. However, this method is more complex than Lund's method.

All the above wind retrieval methods show satisfactory results for radar images collected under rain-free conditions. However, large discrepancies appear when applying these methods to rain-contaminated images [44]. Rain has dual effects on wind waves, causing additional waves in the capillary-gravity/capillary wave range [45, 46] and damping waves in gravity wave range [47–49]. The effect of rain can be different under different wind speeds [50–54]. The interaction between electromagnetic waves and the additional rain-induced waves enhance radar backscatter. Moreover, the peak of the radar backscatter in the upwind direction may be contaminated and difficult to be identified. As a result, the accuracy of the retrieved wind direction will drop, and wind speeds will be overestimated using existing methods [44].

To improve wind speed retrieval accuracy under rain conditions, Huang *et al.* [55] proposed an algorithm that separately trains third-order polynomials with rain-free and rain-contaminated data. To some extent, this algorithm improved the accuracy of the retrieved wind speeds from rain-contaminated images. However, the retrieved wind speeds still have large discrepancies in rain-contaminated periods, since rain-induced backscatter may not increase linearly with wind speed. Moreover, using two

sets of data for training may not be efficient for practical application. Finally, since the method is designed for wind speed, no improvement regarding wind direction was made.

1.3 The Scope of the Thesis

The main content of this thesis is to present methods for retrieving wind information from X-band marine radar data collected under rain conditions. With an aim of mitigating the limitations of existing methods under rain conditions, a wind direction retrieval method is proposed. The method results in an improvement of 25.1° in the wind direction retrieval from rain-contaminated images and maintains the same accuracy as the curve fitting method in [21] under rain-free conditions. In addition, two approaches for improving the wind speed retrieval accuracy under rain conditions are presented. In order to verify these methods, X-band marine radar data collected by Defence Research and Development Canada (DRDC) in 2008 were employed.

The thesis is organized as follows:

In Chapter 2, the new wind direction retrieval algorithm, which involves wavenumber domain analysis, is presented and compared with a method in [21].

Two wind speed retrieval algorithms are presented in Chapter 3. One of them is an extension of the wavenumber-domain-based wind direction approach discussed in Chapter 2. The other algorithm involves the mitigation of the rain effects by applying the gamma correction [56] on rain-contaminated images. Both of these algorithms are compared with the wind speed retrieval method in [21] using shipborne data collected under rain and rain-free conditions.

A summary of the thesis and a few suggestions for future work are presented in Chapter 4.

Chapter 2

Wind Direction Retrieval from

X-band Marine Radar Data

In this chapter, a new algorithm which can be used to retrieve wind direction from both rain-contaminated and rain-free radar images is proposed. An overview of the data used in this chapter is shown in Section 2.1. A brief review of the traditional curve-fitting based method which will be used for the purpose of comparison is presented in Section 2.2. The new wind direction retrieval method is introduced in Section 2.3. In Section 2.4, experimental results are presented and discussed. A chapter summary is given in Section 2.5.

2.1   Data Overview

The data utilized in this chapter were collected by a shipborne radar named Decca. The dataset contain 48,004 images, and was provided by Defence Research and Development Canada (DRDC). The experiments were conducted on the Canadian Navy

Table 2.1: Decca Radar Parameters

Parameters	Values
Frequency	9.41 GHz
Sampling Frequency	20 MHz
Range Resolution	7.5 m
Measurement Range	240 - 2160 m
Antenna Rotation Period	2 s

research ship CFAV Quest during Nov. 26-29, 2008. The location of the experiment was about 220 km from the coast of Halifax ($42°30'$ N, $62°5'$ W), with a water depth of about 200 m. The 9.41 GHz HH-polarized Decca radar and two anemometers were installed on the ship. The radar was mounted 54 ft above the sea surface. The sampling frequency of the radar was 20 MHz. The data was recorded for the range of 240 m to 2160 m from the radar, with a range resolution of 7.5 m. The parameters of the Decca radar are summarized in Table 2.1. The radar was connected to the Wave Monitoring System (WaMoS II) [60]. This system digitizes radar backscatter into 8-bit binary numbers corresponding to image intensity from 0 to 255. The antenna rotation speed of the Decca radar is 28 rpm. Thus, the system collected one image every two seconds. An image from the Decca dataset is shown in Fig. 2.1 (a).

2.2 Curve Fitting Based Method

The curve-fitting-based method [21] is one of the most widely used methods for retrieving wind information from X-band marine radar images, such as that shown in
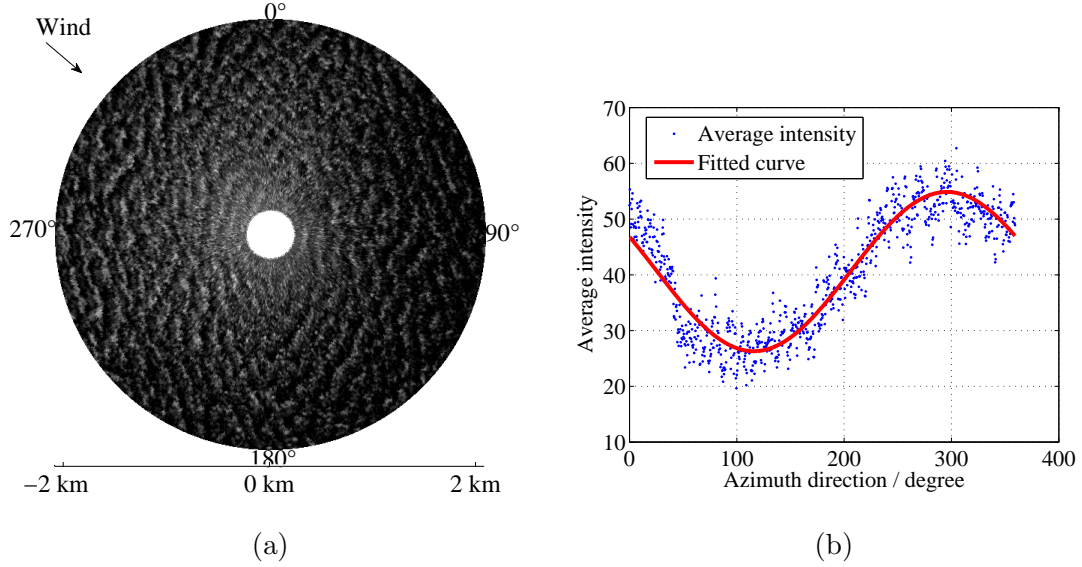
Figure 2.1: (a) A radar image collected under rain-free conditions (obtained on 01:23, Nov. 28, 2008); (b) curve fitting results according to the curve fitting method in [21] for the image shown in (a).

Fig. 2.1 (a). According to this method, radar image intensities are first averaged according to each azimuth direction. The average intensity of each azimuth direction is shown as the blue dots in Fig. 2.1 (b). These average intensity data are then curve fitted by the sinusoidal function [21]

$$\sigma_\theta = a_0 + a_1\cos^2(0.5(\theta - a_2)) \tag{2.1}$$

where σ_θ is the average intensity in azimuth direction θ, and a_0, a_1, and a_2 are parameters that may be determined by the least-squares fitting. The fitted curve is shown in red in Fig. 2.1 (b). Wind direction is determined as the peak of the fitted curve, and in this figure the direction is almost 296°.

11
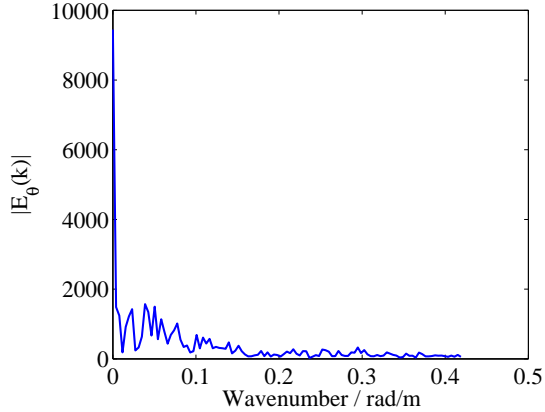
Figure 2.2: Wavenumber spectrum of data in one azimuth

2.3 Wavenumber-domain-based Method

Unlike existing methods, the proposed algorithm is based on the analysis of radar backscatter in the wavenumber domain rather than the spatial domain. The backscatter samples in each azimuth are Fourier transformed into the wavenumber domain to generate the wavenumber spectrum [57, 58]

$$E_\theta(k) = \sum_{n=0}^{N-1} I_\theta(n) e^{-j\frac{2\pi}{N}kn} \tag{2.2}$$

where N is the total number of backscatter samples (i.e. image pixels intensities) in one azimuth, $I_\theta(n)$ is nth pixel intensity in azimuth direction θ, and $E_\theta(k)$ is the spectral value of wavenumber k. An example of the wavenumber spectrum for one azimuth is shown in Fig. 2.2. Two different kinds of information may be obtained from this spectrum. One of them is $|E_\theta(0)|$, the spectral magnitude for $k = 0$. From Eq. (2.2), it can be inferred that $|E_\theta(0)|$ represents the summation of $I_\theta(n)$. In other words, the spectral value of the zero wavenumber component equals to the pixel intensity sum in azimuth direction θ. Another kind of information is associated with

12

the spectral components over wavenumber range [0.01, 0.2] rad/m, corresponding to waves with wavelengths between 31 m to 628 m ($\lambda = 2\pi/k$). These spectral points result from intensity variation and could be a reflection of surface wave signatures. It should be noted that any wavenumber range containing the most significant spectral points excluding the zero-wavenumber component is valid. The range is set to be [0.01, 0.2] since it yields satisfactory results.

As has been found in the literature, the effect of rain is different according to different wind speeds [50–54]. Thus, different spectral components should be employed for wind direction retrieval from different kinds of images. The details follow.

2.3.1   Low Wind Speed Rain Cases

A rain-contaminated image collected under low wind speeds is shown in Fig. 2.3 (a). After performing the Fourier transform on the data along each azimuth, full wavenumber spectra may be obtained for all azimuth directions. For the image shown in Fig. 2.3 (a), spectral points with $k \in [0.01, 0.2]$ are selected and shown in Fig. 2.3 (b). To simplify further calculation, a normalization process is then implemented by dividing every spectral value with the maximum spectral value at wavenumber zero of all azimuths in the image.

As it has been found previously [44], for rain-contaminated radar images collected under low wind speed conditions, the dependence between backscatter intensity and azimuth is reduced. Thus, the intensity might not have a single peak in the upwind direction, in which case $|E_\theta(0)|$ cannot be utilized for wind direction retrieval. On the other hand, surface wave signatures may still be observed in the upwind direction

13

(see Fig. 2.3 (a)). Similarly, high spectral values present themselves in the upwind direction in the wavenumber spectrum with $k \in [0.01, 0.2]$ (see Fig. 2.3 (b)). To identify surface wave signatures in the wavenumber domain, an integral of the normalized spectra over the wavenumber range [0.01, 0.2] is calculated for each azimuth direction. For azimuth direction θ,

$$S_\theta = \int_{0.01}^{0.2} |E_\theta(k)| \, dk. \tag{2.3}$$

$|E_\theta(k)|$ is the spectral magnitude of wavenumber component k. Then, S_θ is curve-fitted by the sinusoidal function

$$S_\theta = a_0 + a_1 \cos^2(0.5(\theta - a_2)) \tag{2.4}$$

proposed in [21], where a_0, a_1, and a_2 are parameters which may be determined by least-squares fitting. The fitted result for the data shown in Fig. 2.3 (a) is displayed in Fig. 2.3 (d). Wind direction is determined at the peak of the fitted curve and found to be 254°, a difference of 12° from the anemometer-measured wind direction. However, wind direction retrieved using the curve fitting based method in [21] is 87° (shown in Fig. 2.3(c)). This may be because the radar image in Fig. 2.3 (a) was significantly affected by rain and the dependence of backscatter intensity on wind direction has been altered.

A large deviation from the general trend in the average intensities (blue dots) is seen near 310° in Fig. 2.3 (c). This deviation always appears between the beginning and the end of the scan of an image. Since the time gap between these two pulses is about 2 seconds, the corresponding scattering may vary, especially under rain conditions. The deviation in rain-free data is not so obvious since purely wave-induced scattering varies little within 2 seconds.
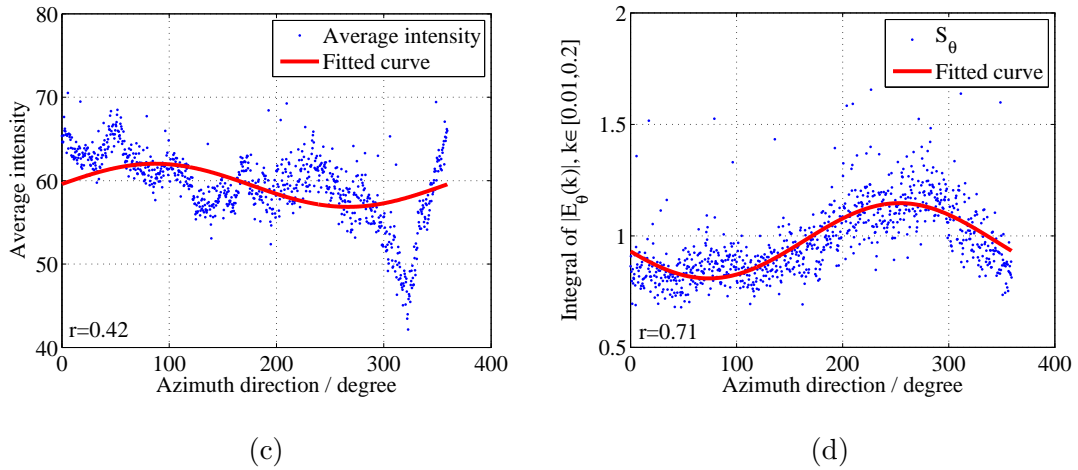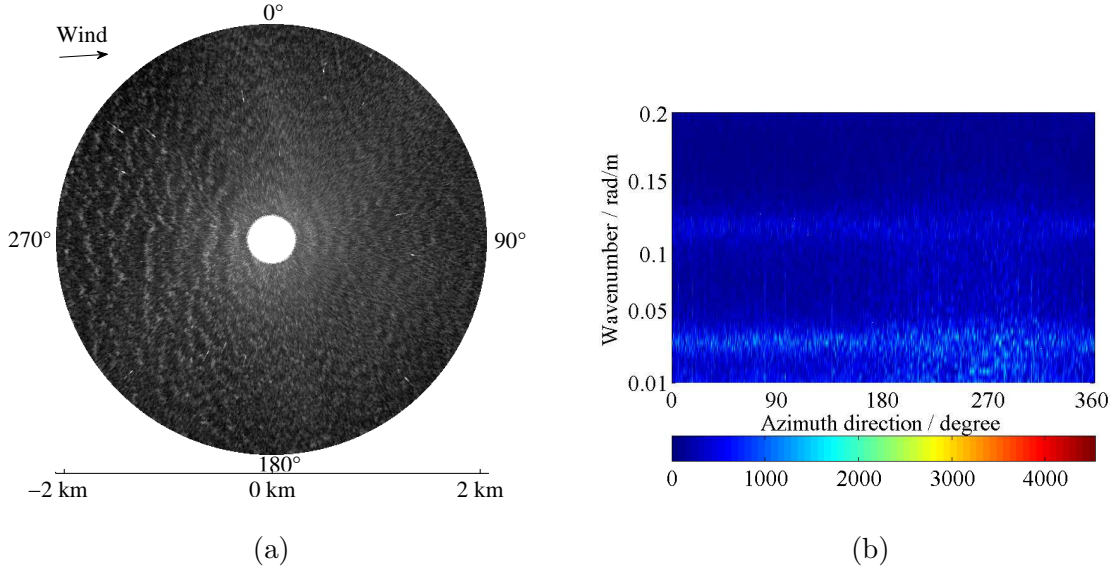
Figure 2.3: (a) A rain-contaminated image collected at low wind speed conditions (obtained on 05:24, Nov. 27, 2008), wind direction measured by anemometers: 266°; (b) wavenumber spectra with $k \in [0.01, 0.2]$ for the image shown in (a); (c) curve fitting results using the curve fitting method in [21] for the image shown in (a) (the retrieved wind direction is 87°); (d) curve fitting results using the proposed method for the image shown in (a) (the retrieved wind direction is 254°). r represents correlation coefficient. The correlation coefficient is a measure of the strength of the linear relationship between two variables, and is defined as the covariance of the variables divided by the production of their standard deviations.

15
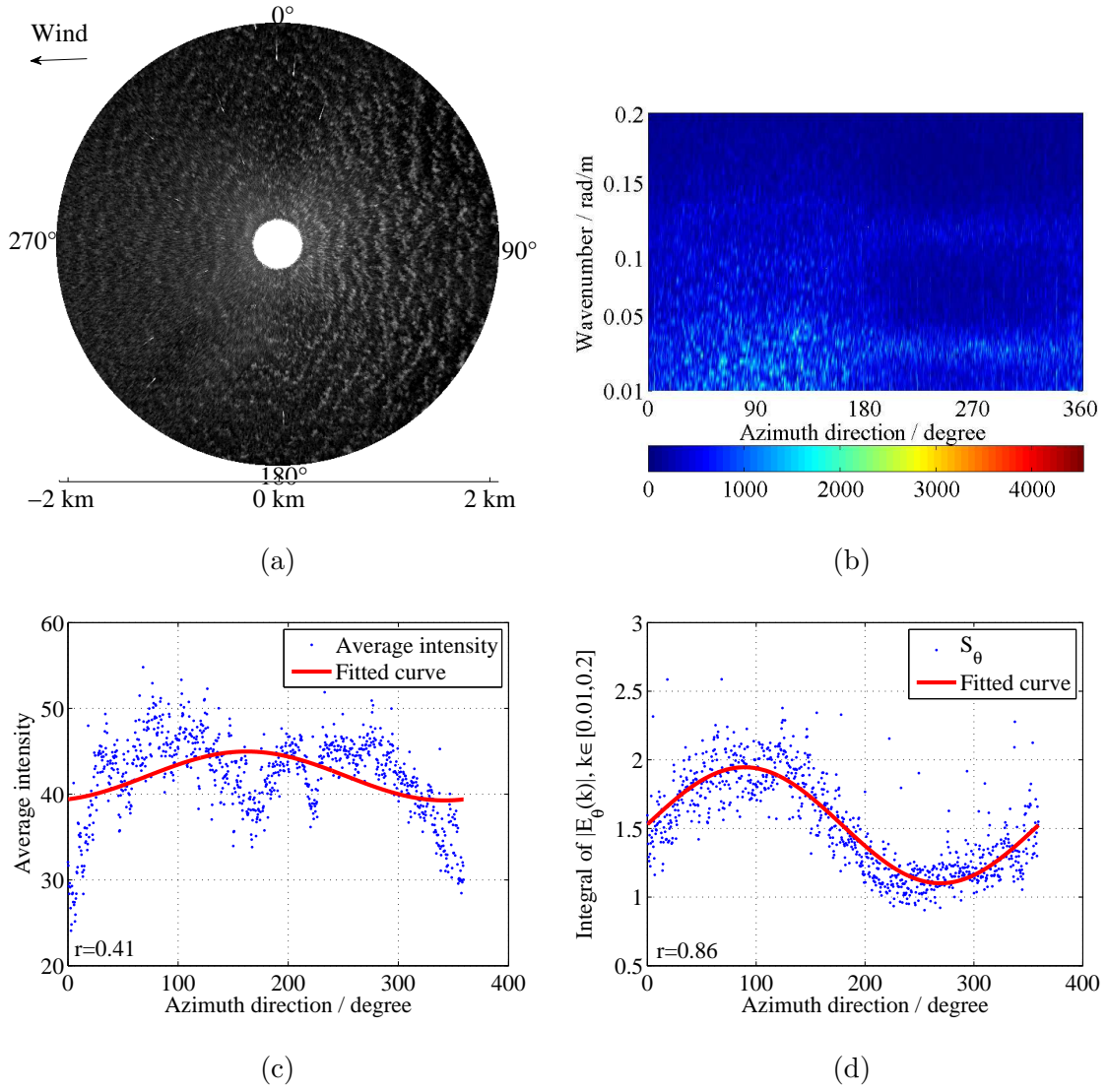
Figure 2.4: (a) An image partly contaminated by rain (rain does not cover the upwind direction), collected under low wind speeds on 01:53, Nov. 27, 2008; wind direction measured by anemometers: 89°; (b) wavenumber spectra with $k \in [0.01, 0.2]$ for the image shown in (a); (c) curve fitting results using the curve fitting method in [21] for the image shown in (a) (the retrieved wind direction is 162°); (d) curve fitting results using the proposed method for the image shown in (a) (the retrieved wind direction is 89°). r represents correlation coefficient.

16
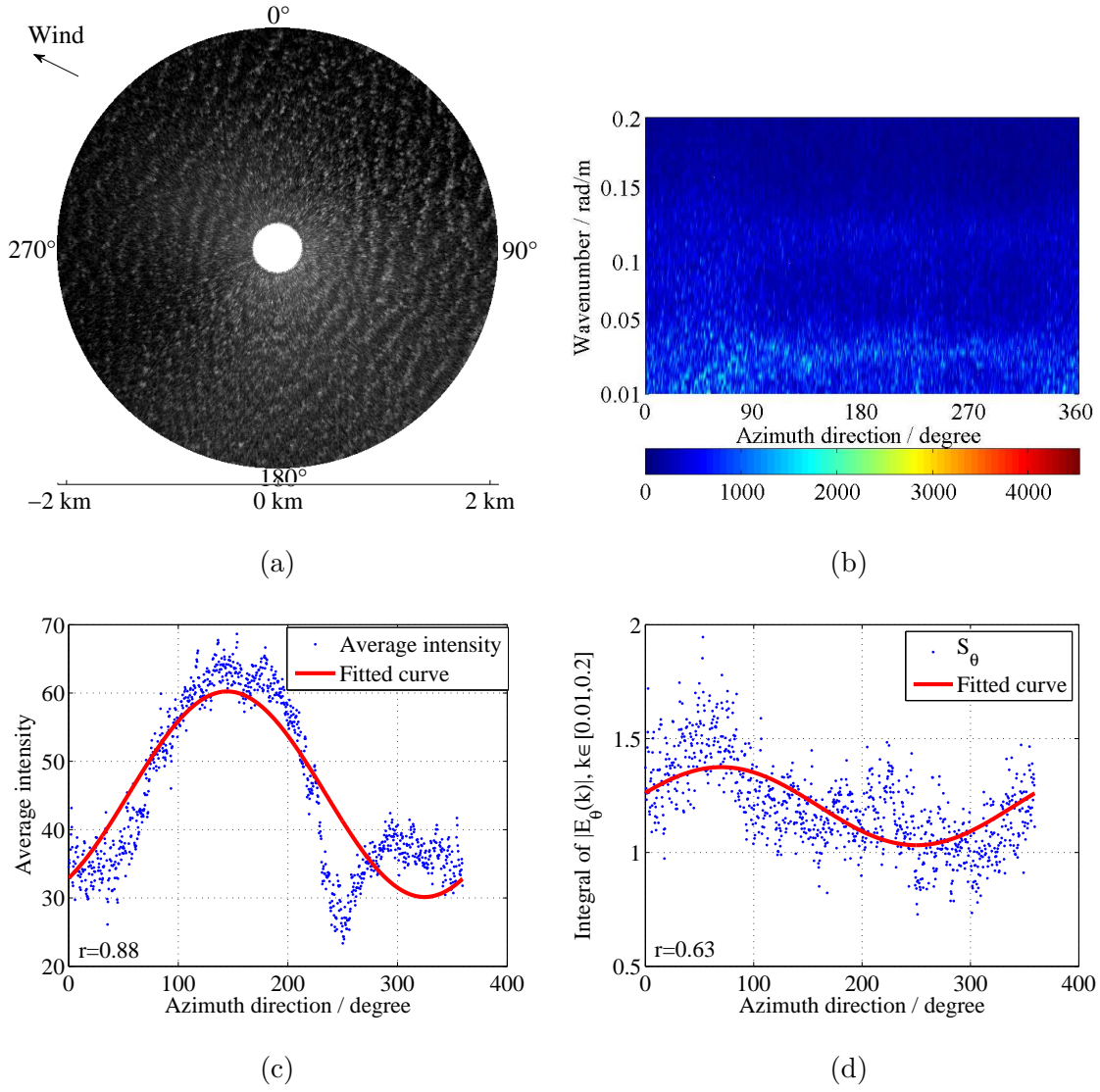
Figure 2.5: (a) An image partly contaminated by rain (rain covers the upwind direction), collected under low wind speeds on 18:34, Nov. 28, 2008; wind direction measured by anemometers: 131°; (b) wavenumber spectra with $k \in [0.01, 0.2]$ for the image shown in (a); (c) curve fitting results using the curve fitting method in [21] for the image shown in (a) (the retrieved wind direction is 144°); (d) curve fitting results using the proposed method for the image shown in (a) (the retrieved wind direction is 70°). r represents correlation coefficient.

It may be observed that the image shown in Fig. 2.3 (a) is comprehensively contaminated by rain, i.e. rain appears in all azimuth directions. In actual measurements, there are images partly contaminated by rain. The performance of the proposed method on such images depends on the locations of the rain areas. For example, for the partly contaminated image shown in Fig. 2.4 (a), where rain appears in the down wind direction instead of the upwind direction, the result of the proposed method is very promising (see Fig. 2.4 (d)). However, when the image is partly rain-contaminated and rain occurs in the upwind direction only (shown in Fig. 2.5 (a)), the accuracy of the retrieved wind direction using the proposed method decreases (see Fig. 2.5 (d)). A possible reason for this is that when rain occurs in the upwind direction only, it reduces the wave signatures as well as the upwind peak of S_θ. S_θ in the upwind direction becomes lower than in other directions, and its peak is difficult to identify since wave signatures in other directions are not contaminated significantly. Fortunately, partly contaminated images exist within the first or last three minutes of the rain period. The method works for most rain-contaminated images collected under low wind speeds (more details are given in Section 2.3.3).

2.3.2 High Wind Speed Rain Cases

Under high wind speeds, the upwind-downwind radar return ratio may decrease to less than 1.5 [59]. Since wind forcing dominates the generation of surface roughness in this case [49, 54], rain can cause additional radar backscatter but may not blur surface wave signatures. Instead, signatures in the downwind direction may become comparable to the upwind direction (see Fig. 2.6 (a)). A possible reason for this
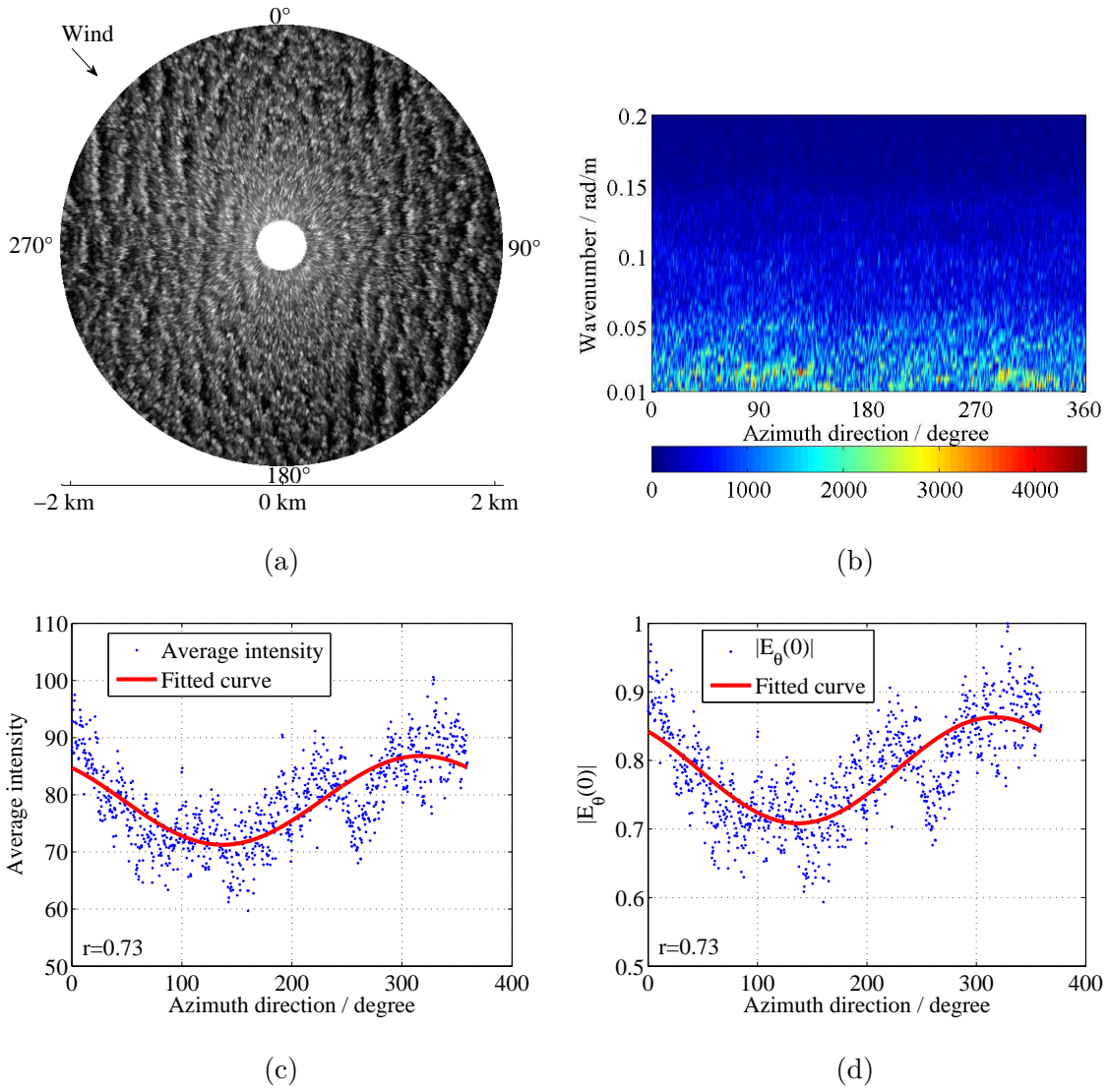
Figure 2.6: (a) A rain-contaminated image collected at high wind speed conditions (obtained on 09:50, Nov. 27, 2008); wind direction measured by anemometers: $317°$; (b) wavenumber spectra with $k \in [0.01, 0.2]$ for the image shown in (a); (c) curve fitting results using the curve fitting method in [21] for the image shown in (a) (the retrieved wind direction is $317°$); (d) curve fitting results using the proposed method for the image shown in (a) (the retrieved wind direction is $317°$). r represents correlation coefficient.

may be that rain causes additional wave breaking in downwind direction. On the corresponding wavenumber spectrum with $k \in [0.01, 0.2]$, high spectral values may present in the upwind direction as well as the downwind direction (see Fig. 2.6 (b)). Thus, S_θ can not be utilized for wind direction retrieval in this case. On the other hand, since wind force dominates, the intensity dependence on the azimuth direction may not be altered. Thus, the spectral values at zero wavenumber, i.e. $|E_\theta(0)|$, are chosen for curve-fitting, i.e.,

$$|E_\theta(0)| = a_0 + a_1 \cos^2(0.5(\theta - a_2)) \tag{2.5}$$

It should be noted that this scheme is analogous to the curve fitting based method in [21], since $|E_\theta(0)|$ represents the normalized pixel intensity sum of azimuth direction θ. In [21], the averaged pixel intensity along θ was used in the left-hand side of Eq. (2.5). For the rain-contaminated image shown in Fig. 2.6 (a), the fitted results using the curve fitting method in [21] and the new method are shown in Fig. 2.6 (c) and Fig. 2.6 (d), respectively. The retrieved wind directions using both methods are $317°$, which are exactly the same as the anemometer-measured results.

2.3.3 Rain-free Cases

For rain-free cases, the wind force dominates. Both S_θ and $|E_\theta(0)|$ have single peaks in the upwind direction and may be used for wind direction retrieval (see Fig. 2.7 (a), (b)). After applying the new method with S_θ and $|E_\theta(0)|$ to all rain-free data in this study, it was found that the root mean square error (RMSE) in the wind direction retrieved using $|E_\theta(0)|$ is $4°$ lower than that with S_θ. Thus, $|E_\theta(0)|$ is recommended for wind direction retrieval from rain-free data. For the rain-free image shown in
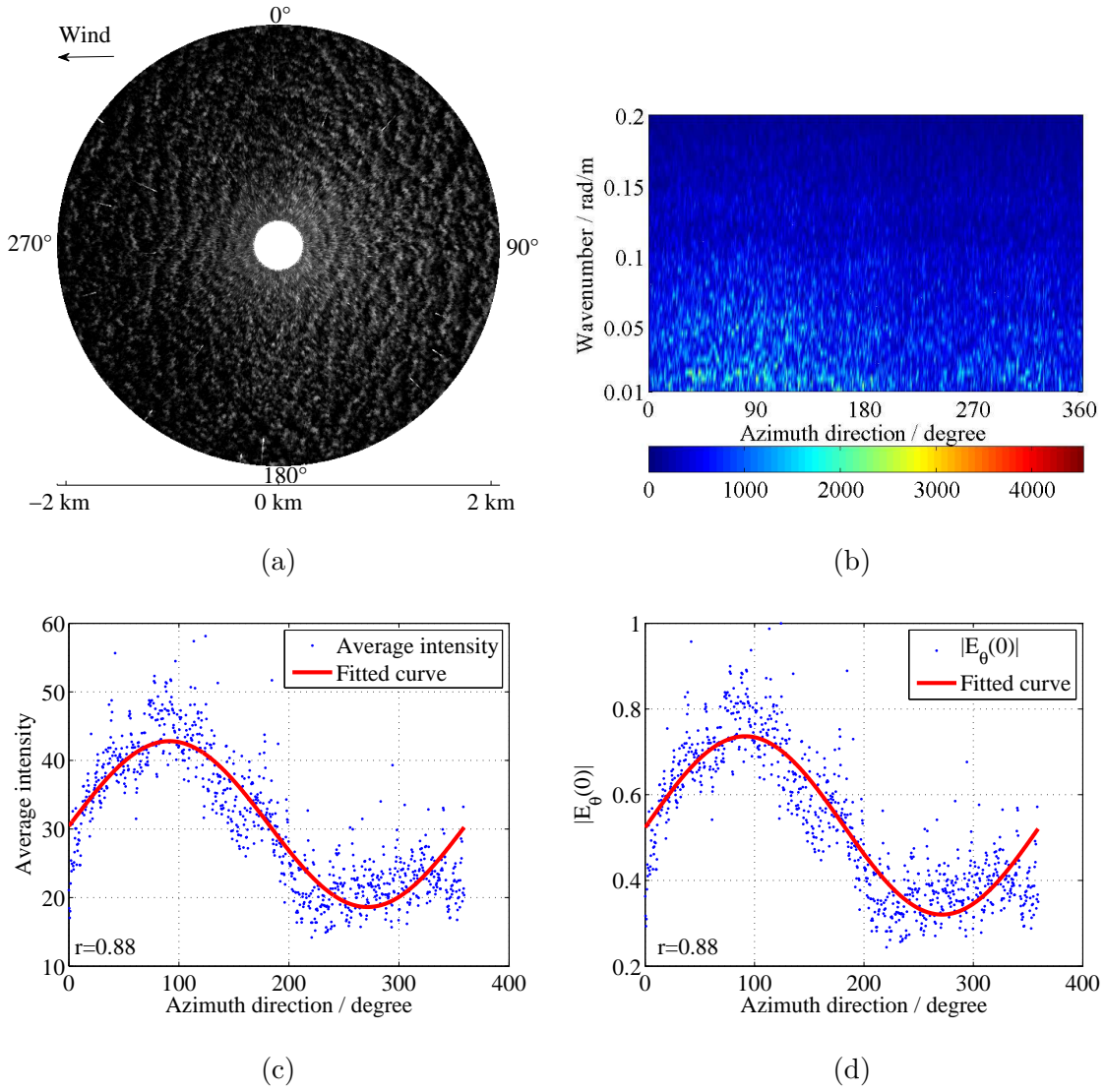
Figure 2.7: A rain-free image (obtained on 00:51, Nov. 27, 2008); wind direction measured by anemometers: 90°; (b) wavenumber spectra with $k \in [0.01, 0.2]$ for the image shown in (a); (c) curve fitting results using the curve fitting method in [21] for the image shown in (a) (the retrieved wind direction is 91°); (d) curve fitting results using the proposed method for the image shown in (a) (the retrieved wind direction is 91°). r represents correlation coefficient.

Fig. 2.7 (a), the retrieved wind directions using the curve fitting based method in [21] and $|E_\theta(0)|$ are 91° (see Fig. 2.7 (c), (d)), with a 1° difference from the anemometer-measured wind direction.

2.4 Results

2.4.1 Image Classification

Before applying the proposed method, it is first necessary to classify the radar images. Rain-contaminated images may be identified based on zero pixel percentage (ZPP) [21], which is defined as the percentage of the overall number of image pixels with intensities below 5. If the ZPP of an image is smaller than 10%, such an image will be regarded as a rain-contaminated image [61]. According to this classification, five periods in the selected radar sequence were found to be rainy periods. In order to distinguish the rain-contaminated images collected under low wind speeds from those under high wind speeds, a parameter referred to as the high pixel percentage (HPP) is defined as the percentage of the overall number of pixals with intensities higher than 100. If the HPP of a rain-contaminated image is lower than 15%, the image will be identified as belonging to the low wind speed rain cases, otherwise it will be classified as rain-contaminated data under high wind speeds. This HPP threshold approximately corresponds to a wind speed of 8 m/s. It should be noted that the wind speeds are only classified as low or high, and no transitional range is used in this study. The ZPP and HPP results are shown in Fig. 2.8 (a). The data from 03:32 to 03:44 Nov. 27 and from 23:40 Nov. 28 to 01:16 Nov. 29 yielded low-clutter images

Table 2.2: Image Classification Results

Image type	Number	Percentage
Low wind speed rain cases	4,861	10.12%
High wind speed rain cases	4,050	8.44%
Low clutter images	1,907	3.97%
Rain-free non-low-clutter images	37,186	77.45%

(ZPP higher than 60 %). No data was collected from 04:05 to 11:15 Nov. 28.

Based on the classification method described above, the number and percentage of different categories of images are shown in Table 2.2. By excluding the low-clutter images due to system error or very low wind speeds, the numbers of rain-free and rain-contaminated images were found to be 37,186 and 8,911, respectively. Among the rain-contaminated data, 4,861 images are identified as low wind speed cases, corresponding to data in the time periods of 01:47-03:30 and 04:44-05:48 Nov. 27, 16:50-19:23 Nov. 28, and 06:35-09:04 Nov. 29. These classification results coincide with the anemometer-measured wind speeds (see Fig. 2.9 (a)) and rain gauge-measured rain rates (see Fig. 2.9 (b)).

2.4.2 Wind Direction Retrieval Results

Both the curve fitting based method in [21] and the proposed method were applied to the aforementioned radar data. To obtain better accuracy, data utilized for low wind speed rain cases and other cases are in the range of 540-2160 m and 690-2160 m, respectively. The averaged wind directions of the two anemometers were utilized as a
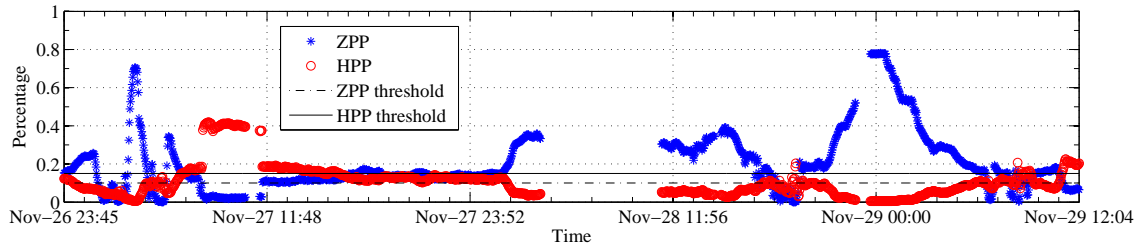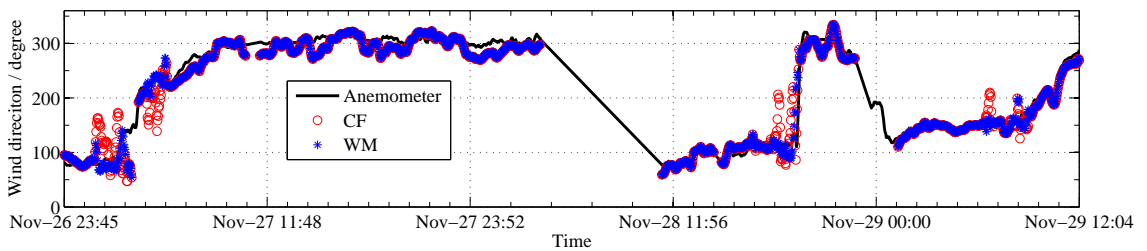
Figure 2.8: Results: (a) Zero Pixel Percentage (ZPP) and High Pixel Percentage (HPP); (b) retrieved wind directions, RMSE of the curve fitting based method in [21] (CF) for low-wind-speed rain-contaminated images: 46.7°, RMSE of the wavenumber-domain-based method (WM) for low-wind-speed rain-contaminated images: 21.6°.
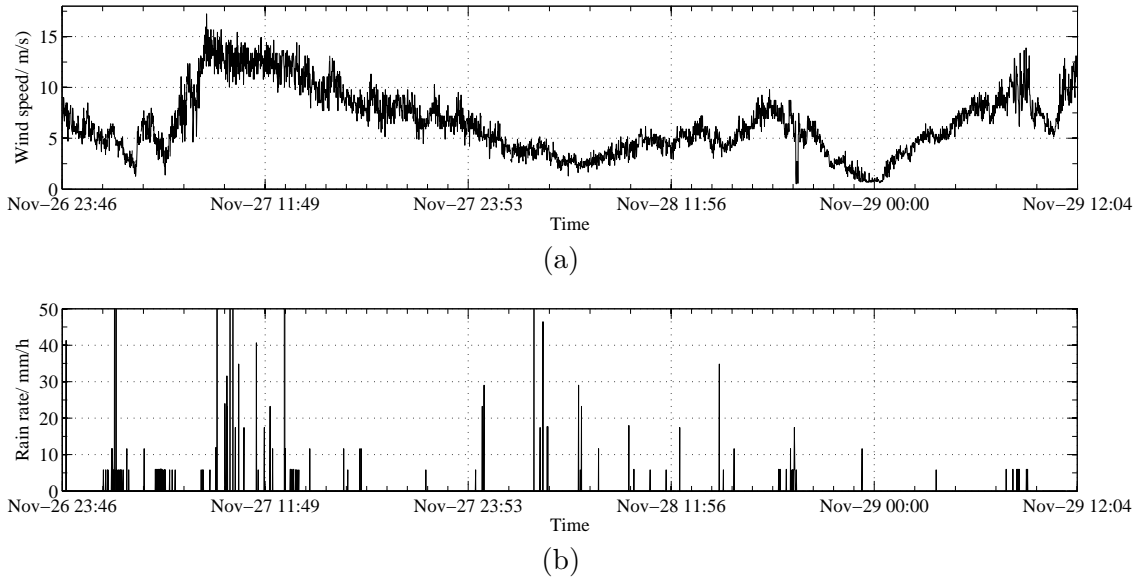
Figure 2.9: (a) Measured wind speeds; (b) Measured rain rates

reference for comparison with radar results. Retrieved wind directions were averaged every ten minutes and are shown in Fig. 2.8 (b).

From Fig. 2.8 (b), it can be seen that the wind directions retrieved using the curve fitting based method in [21] agree well with anemometer data except for the four periods associated with rain and low wind speeds (see Figs. 2.8- 2.9). The root mean square error (RMSE) of wind direction derived using the curve fitting based method for these periods is 46.7° while the RMSE using the new method is only 21.6° (see Table 2.3). Wind direction retrieval accuracy for low-wind-speed rain cases has been improved by 25.1° with the new method. It should be noted that satisfactory wind directions were obtained using the proposed method from 4,733, i.e. 97.4%, of the 4,861 rain-contaminated images. The errors in the wind direction results obtained from the remaining 128 images are relatively large since only surface wave signatures in the upwind direction are contaminated. For rain-contaminated images collected

25

Table 2.3: Wind Direction Retrieval Error Statistics: RMSEs

Methods/ Data type	Rain-contaminated Data	Rain-free Data
Curve Fitting Based Method in [21]	46.7°	14.9°
The Wavenumber-domain-based Method	21.6°	14.9°

under high wind speed conditions and rain-free images, retrieved wind directions using the two methods are the same. For all the data considered in this study, the RMSEs of the curve-fitting-based method and the wavenumber-domain-based method are 20.3° and 15.8°, respectively.

2.5 Chapter Summary

A new method for retrieving wind direction from both rain-contaminated and rain-free X-band nautical radar images has been proposed. The method is designed based on the analysis of radar backscatter in the wavenumber domain. For rain-contaminated images collected under low wind speeds (i.e. less than 8 m/s), spectral points corresponding to wavenumber components in the range of [0.01, 0.2] rad/m are used for wind direction retrieval. For rain-free and rain-contaminated data collected under high wind speeds, the spectral points at wavenumber zero are employed.

The new method has been applied to 48,004 X-band radar images collected in the North Atlantic Ocean. The radar-derived wind directions are compared with those measured by anemometers. The comparison shows that the RMSE of the wind direction retrieved from rain-contaminated data associated with low wind speeds is reduced by 25.1° with the new method. For rain-free images and high wind speed

rain cases, this method maintains the same accuracy as the curve fitting method in [21]. Based on the data available, no definite relationship between the rain rate and the spectral strengths at wavenumber 0 or above 0.2 rad/m has been observed since backscattering intensity depends on both wave and rain conditions.

Chapter 3

Wind Speed Retrieval from

X-band Marine Radar Data

In this chapter, two new approaches for wind speed retrieval from rain-contaminated and rain-free images are presented. Firstly, an overview of the data used in this chapter is provided in Section 3.1. Then, the traditional curve fitting based method for wind speed estimation is briefly reviewed in Section 3.2. The first new wind speed retrieval method, which is based on the analysis in the wavenumber domain, is introduced in Section 3.3. In Section 3.4, another wind speed retrieval method which is based on the gamma correction in the spatial domain is introduced. Results and comparison of these methods are shown in Section 3.5. The summary of this chapter is shown in Section 3.6.

3.1 Data Overview

Two datasets collected by Decca and Furuno radars were used to verify the proposed methods. Both of them were provided by Defence Research and Development Canada (DRDC). A detailed description of the Decca dataset is found in Section 2.1. The Furuno dataset contains 68,992 images, which were also collected by a HH-polarized shipborne radar operating at 9.41 GHz. The radar was mounted 72 ft above the sea surface. The radar's measurement range is from 240 m to 2160 m, with a range resolution of 7.5 m. The WaMoS II system was connected to the radar and was used to digitize radar backscatter into 8-bit unsigned integers ([0, 255]). The Furuno system differs from the Decca in two aspects. Firstly, the antenna rotation speed of the Furuno system is 40 rpm while the rotation speed is 28 rpm in Decca system. Thus, the Furuno system collected one image every 1.5 seconds. Another difference between the Furuno and Decca systems is that in the former the data were processed by a rain-filter. Thus, the overall intensity of an image in the Furuno dataset is lower than that in the Decca dataset. The parameters of the Furuno radar are shown in Table 3.1. An image from the Furuno dataset is shown in Fig. 3.1. It may be seen that its intensities are much lower than those shown in Fig. 2.1 (a) or Fig. 2.7 (a).

In this chapter, the Decca dataset is used to test and compare the performance of the two proposed wind speed retrieval methods with the curve-fitting-based method in [21]. The Furuno dataset is only employed to test the performance of the wavenumber domain method. The reason for this is that the rain effect in pre-filtered images is not as obvious as that in non-filtered images. Thus, rain-contaminated image in the Furuno dataset may not be correctly selected using ZPP. As a result, the gamma-

Table 3.1: Furuno Radar Parameters

Parameters	Values
Frequency	9.41 GHz
Sampling Frequency	20 MHz
Range Resolution	7.5 m
Measurement Range	240 - 2160 m
Antenna Rotation Period	1.5 s
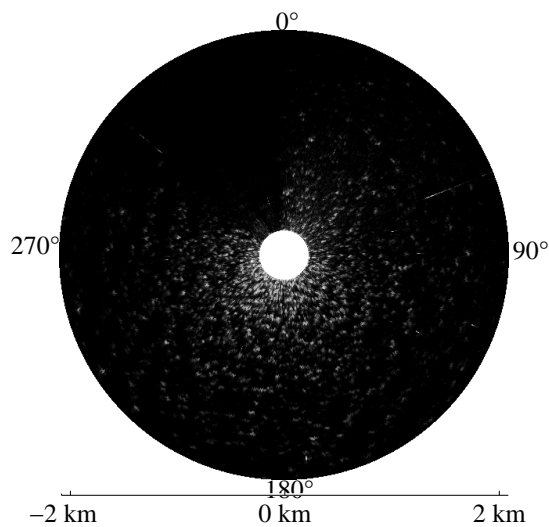
Figure 3.1: An image in Furuno dataset, collected on 12:30, Dec. 01, 2008.

correction-based method, which requires correct identification of rain-contaminated images, could not be applied to the Furuno dataset.

3.2 Curve-fitting-based Method

Sea surface wind information retrieval from X-band marine radar data is based on the observation that the normalized radar backscatter is related to the sea surface wind vector. The curve-fitting-based method proposed in [21] relates the average radar backscatter intensity of an image to the measured wind speed using a third-order polynomial. The average intensity σ_{ws} is defined as

$$\sigma_{ws} = \frac{1}{2\pi} \int_0^{2\pi} \left(a_0 + a_1 \cos^2(0.5(\theta - a_2)) \right) d\theta. \tag{3.1}$$

It may be seen that σ_{ws} is actually the average of σ_θ shown in Eq. 2.1. The relationship between σ_{ws} and wind speed w may be written as

$$\sigma_{ws} = b_0 + b_1 w + b_2 w^2 + b_3 w^3 \tag{3.2}$$

where b_0, b_1, b_2 and b_3 are parameters to be determined by least-squares fitting. An example of the fitted relationship for σ_{ws} and wind speed is shown in Fig. 3.2. The limitation of this method is that it can be applied to rain-free images only. The retrieved wind speeds are usually higher than the measured ones, since rain introduces additional backscatter.
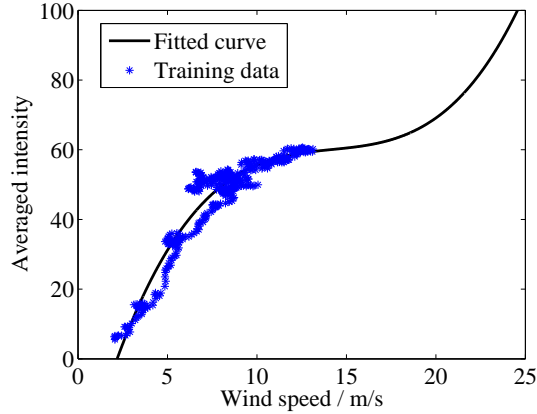
Figure 3.2: A scatter plot of wind speed and average intensity. (Rain-free data with wind speeds > 2 m/s for the time periods 12:00 p.m. - 23:00 p.m. Nov. 27 and 00:30 a.m. - 07:00 a.m. Nov. 29 were used for training

3.3 Wavenumber-domain-based Method

Unlike existing algorithms, the first new wind speed retrieval method is implemented based on the analysis of wavenumber spectra rather than image intensity directly [62].

As for the wind direction retrieval method introduced in Chapter 2, image intensities in each azimuth direction are Fourier transformed into the wavenumber domain by Eq. 2.2. As illustrated in Fig. 2.2, the spectral value at zero wavenumber $|E_\theta(0)|$ reflects the intensity information, since it is a summation of all the pixel intensities in azimuth direction θ. Other components, i.e. $|E_\theta(k)|$ when $k \neq 0$, reflect intensity variation.

To see the difference between the zero wavenumber component and the nonzero wavenumber components, $|E_\theta(k)|$ for $k \neq 0$ in all directions are summed and then

averaged to obtain $S_{nonzero}$ as

$$S_{nonzero} = \frac{1}{2\pi} \int\limits_0^{2\pi} \int\limits_{k_1}^{k_N} |E_\theta(k)| \, dk d\theta \tag{3.3}$$

where k_N is the Nyquist wavenumber, which can be calculated according to the radar range resolution Δr using

$$k_N = \frac{\pi}{\Delta r}. \tag{3.4}$$

k_1 is the first nonzero wavenumber, which can be calculated according to [7]

$$k_1 = \frac{2\pi}{N\Delta r}. \tag{3.5}$$

It may be seen that $S_{nonzero}$ is the average of the nonzero components in the wavenumber spectra. Thus, it represents the overall intensity variation information of an image. $|E_\theta(0)|$ is also averaged with respect to azimuth direction to obtain S_{zero},

$$S_{zero} = \frac{1}{2\pi} \int\limits_0^{2\pi} |E_\theta(0)| \, d\theta. \tag{3.6}$$

S_{zero} actually represents the overall average radar backscatter intensity of an image and it has been used to obtain wind speeds from rain-free images [21, 55]. A scatter plot of S_{zero} and $S_{nonzero}$ is shown in Fig. 3.3. It can be seen that the relationship between S_{zero} and $S_{nonzero}$ is almost linear for rain-free data. This means wind speed may be retrieved using either S_{zero} or $S_{nonzero}$. However, no linear relationship between S_{zero} and $S_{nonzero}$ can be found for rain-contaminated data. It has been confirmed that wind speed will be overestimated if only S_{zero}, i.e. the intensity information, is used [21, 44]. Thus, $S_{nonzero}$, i.e. the intensity variation information, needs to be considered for wind speed estimation from rain-contaminated data.
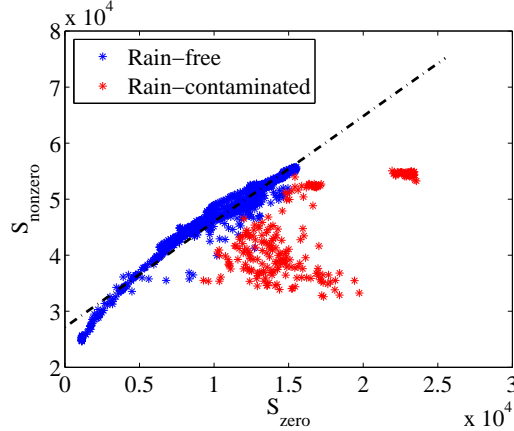
Figure 3.3: Scatter plot of S_{zero} and $S_{nonzero}$.

In this study, both S_{zero} and $S_{nonzero}$ are employed. After obtaining the wavenumber spectrum in every azimuth direction, an integral of $|E_\theta(k)|$ is calculated with respect to azimuth directions and wavenumbers by

$$S = \frac{1}{2\pi} \int\limits_0^{2\pi} \int\limits_0^{k_N} |E_\theta(k)| \, dk d\theta. \tag{3.7}$$

It may be seen that the obtained S equals to the sum of S_{zero} and $S_{nonzero}$. S involves both intensity as well as intensity variation information. Besides, S is very large (a value around ten thousand in our case). To make the further fitting easy, a normalization process, in which S is divided by a scaling factor to reduce it to a value around two or three hundred, is suggested. The scale factor is selected as the maximum pixel intensity 255 in this study.

Another difference in the proposed method from previous methods is that the third-order polynomial is not used as the training function. Although a third-order polynomial could be used to describe the relationship between the radar backscatter intensity and wind speed, it is possible that it will yield incorrect relationships. An example is shown in Fig. 3.4, where the fitted third-order polynomial function de-

34
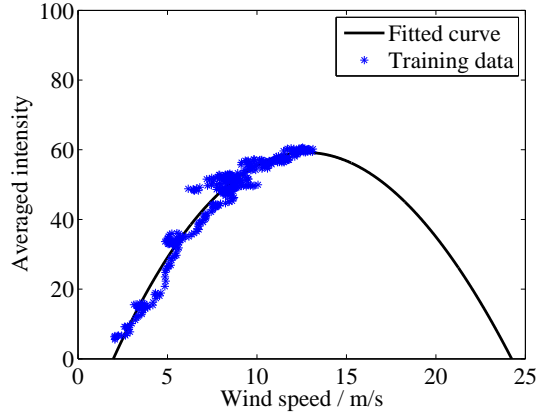
Figure 3.4: Incorrect relationship obtained with a third-order polynomial. (Rain-free data with wind speeds > 2 m/s for the time periods 12:00 p.m. - 21:00 p.m. Nov. 27 and 00:30 a.m. - 07:00 a.m. Nov. 29 were used for training.)

creases when the wind speed is higher than 13 m/s. This contradicts what is seen in actual measurements. Moreover, ambiguity exists in the retrieved wind speeds using such a curve, since two wind speeds (within the meaningful range) will be obtained for each intensity value. In [63], it was found that the cube law fits data collected under low rather than high wind speeds. Instead, a logarithmic function has been used to relate radar backscatter with both low and high wind speeds [64–67]. Thus, a logarithmic function is employed here. The relationship between the spectral integral S and wind speed w can be written as

$$S = a_0 + a_1 \ln(w + a_2) \tag{3.8}$$

where a_0, a_1, a_2 are parameters that can be determined by least-squares fitting S and the reference wind speeds. The fitted curve is then used to determine wind speeds from further measurement of S.

3.4 Gamma Correction Method

The second new wind speed retrieval method investigates radar images in the spatial domain [68]. As noted in Section 3.2, rain causes additional radar backscatters. Thus, the influence of rain should be mitigated in order to retrieve wind speed. The main difficulty of mitigating the rain effect is that it is a nonlinear process. Rain may dampen sea surface waves in the gravity range and enhance waves in the capillary-gravity/capillary range [47–49]. Moreover, the influence of rain varies with wind speeds [50–54]. To reduce the nonlinear effect of rain, the proposed method employs the gamma correction [56]. The detailed process follows.

As shown in Section 2.3.2, rain-contaminated images can be identified using the zero pixel percentage (ZPP) [21, 61]. Two rain-contaminated images collected under low and high wind speeds are shown in Fig. 3.5 (a) and (c), respectively. It is found that under low wind speeds, rain drops blurred sea surface wave signatures (see Fig. 3.5 (a)). Under high wind speeds, the additional rain-induced scatters may make the wave signatures noisy (see Fig. 3.5 (c)). After the rain-contaminated images are identified, a normalization process in which the image intensities are divided by the maximum intensity I_{max} (255 in this study) is applied.

To mitigate the rain influence, a nonlinear correction, i.e. gamma correction, was applied. The gamma correction is typically used in coding and decoding the luminance and tristimulus values in video or image data. For the luminance image data in this study, the gamma corrected intensity I_{out} is expressed as [56]

$$I_{out}(i,j) = (I_{in}(i,j))^{\gamma} \tag{3.9}$$

where I_{in} is the normalized image intensity, and i and j represent the row and column

36
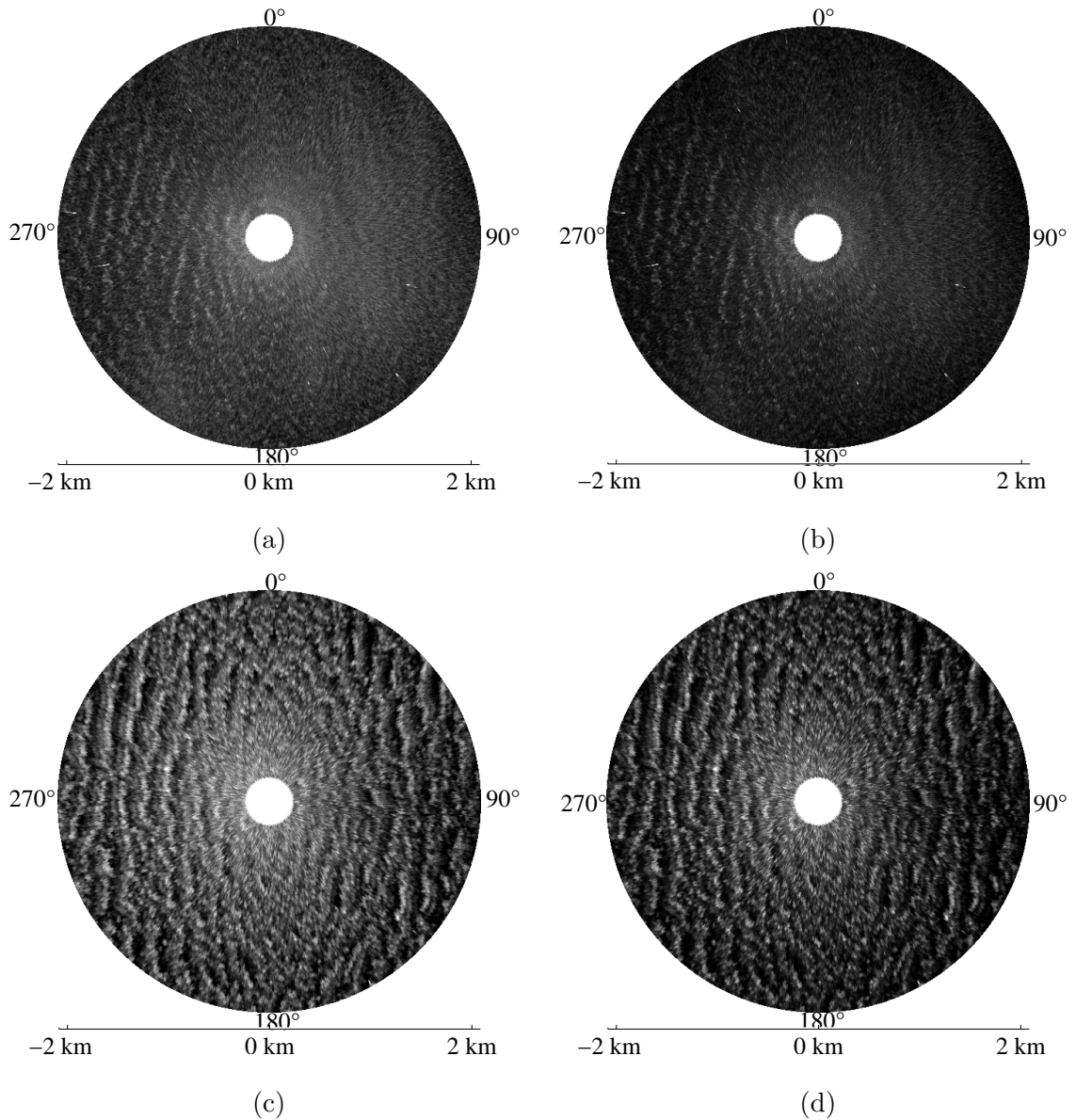
Figure 3.5: (a) A low wind speed (4.7 m/s) rain-contaminated image collected on 05:30, Nov. 27, 2008; (b) image after gamma correction for the image shown in (a); (c) a high wind speed (9.5 m/s) rain-contaminated image collected on 08:36, Nov. 27, 2008; (d) image after gamma correction for the image shown in (c).
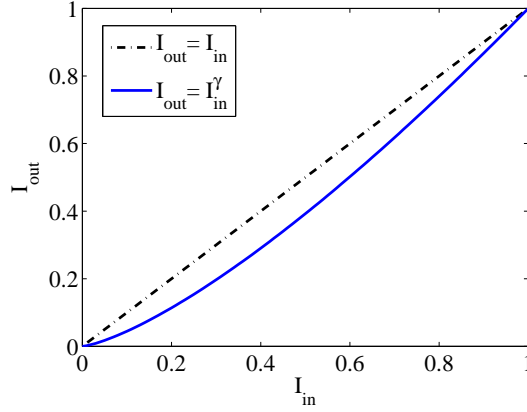
Figure 3.6: The blue line is gamma correction curve where $\gamma = 1.35$, the dot dash line is shown for comparison.

number of the pixel, respectively. The correction factor γ should be selected to reduce the additional scatters caused by rain. Thus, γ should be larger than 1. Besides, the value of γ should not be larger than 1.5 to avoid any over correction. After comparing the result images using different γ values, it was found that the optimal result occurred when γ equals 1.35. This value was selected and used in this study. The relationship between the intensities before and after the gamma correction is shown in Fig. 3.6. For the low and high wind-speed rain-contaminated images shown in Fig. 3.5 (a) and (c), the images obtained after applying the gamma correction are shown in Fig. 3.5 (b) and (d). It may be observed that the rain influence has been reduced in both cases.

The average intensity of the rain-contaminated image is calculated from the gamma-corrected image, and the average of I_{out} is multiplied by I_{max}. The average intensity of the rain-free image is directly calculated from the original image.

Similar to the wavenumber-domain-based method in Section 3.2, a logarithmic

```
                    ┌─────────────────────┐
                    │ Image Classification │
                    └─────────────────────┘
                              │
Rain-free images              │ Rain-contaminated images
          │                   ▼
          │           ┌─────────────────┐
          │           │  Normalization  │
          │           └─────────────────┘
          │                   │
          │                   ▼
          │           ┌─────────────────┐
          │           │ Gamma Correction │
          │           └─────────────────┘
          │                   │
          │                   ▼
          │           ┌─────────────────┐
          │           │ Denormalization │
          │           └─────────────────┘
          │                   │
          │                   ▼
          │   ┌───────────────────────────┐
          └──▶│ Calculate Average Intensity │
              └───────────────────────────┘
                              │
                              ▼
                    ┌─────────────────────┐
                    │ Least-squares fitting │
                    └─────────────────────┘
```
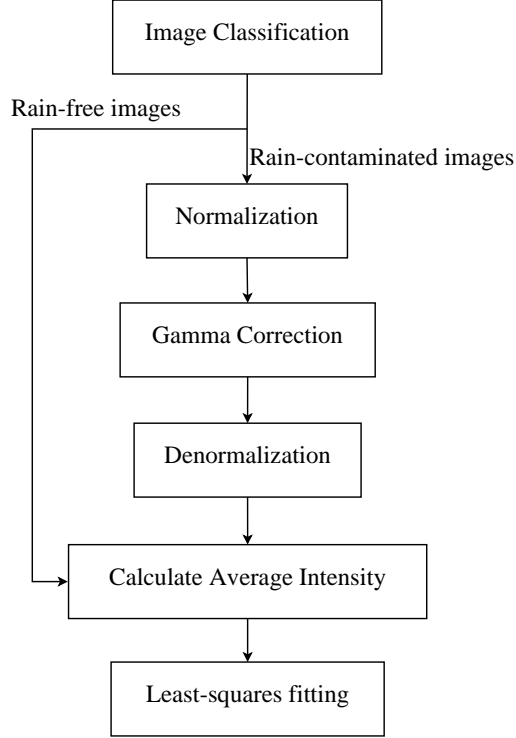
Figure 3.7: A flow chart of the gamma correction method.

function [64–66] is used to relate the average intensity I_{ave} to wind speed w. The logarithmic function may be written as

$$I_{ave} = a_0 + a_1 \ln(w + a_2) \tag{3.10}$$

where a_0, a_1, a_2 are parameters to be determined by least-squares fitting. The fitted curve is then used to determine wind speeds from further collected radar images. The overall flow chart of the gamma correction method is shown in Fig. 3.7.

3.5 Results

3.5.1 Wind Speed Retrieval Results of Decca Dataset

Firstly, both the wavenumber-domain-based wind speed retrieval method and the method incorporating the gamma correction were applied to 48,004 images in the Decca dataset. For the purpose of comparison, the curve-fitting-based method in [21] was also applied. Seventeen and a half hours of rain-free data (obtained under wind speeds higher than 2 m/s) were used to train the relationship between radar backscatter intensities and anemometer-measured wind speeds. These data correspond to the time periods from 12:00 p.m. to 23:00 p.m. on Nov. 27 and 00:30 a.m. to 07:00 a.m. on Nov. 29. The best-fit curves derived using a third-order polynomial according to the curve-fitting-based method in [21] and logarithmic functions according to methods in Section 3.2 and 3.3 are shown in Fig. 3.8 (a), (b) and (c), respectively. The remaining 35.5 hours of data (rain-free and rain-contaminated) were utilized as validation.

The wind speeds retrieved using all three methods, as well as the anemometer measured wind speeds, were averaged every ten minutes and are shown in Fig. 3.9 (a) and (b). The rain rate measured by a rain-gauge is shown in Fig. 3.9 (c). The rain periods include: 01:47-03:30 a.m., 04:44-05:48 a.m. and 07:45-11:32 a.m. on Nov. 27, 16:50-19:23 p.m. on Nov. 28, 06:35-a.m. on Nov. 29. The root mean square errors (RMSEs) of the retrieved wind speeds using all three methods are shown in Table 3.2. Compared with the anemometer-measured wind speeds in these rain periods, the RMSEs of the wind speeds retrieved using the curve-fitting-based method in [21], the proposed wavenumber-domain-based method and the proposed gamma
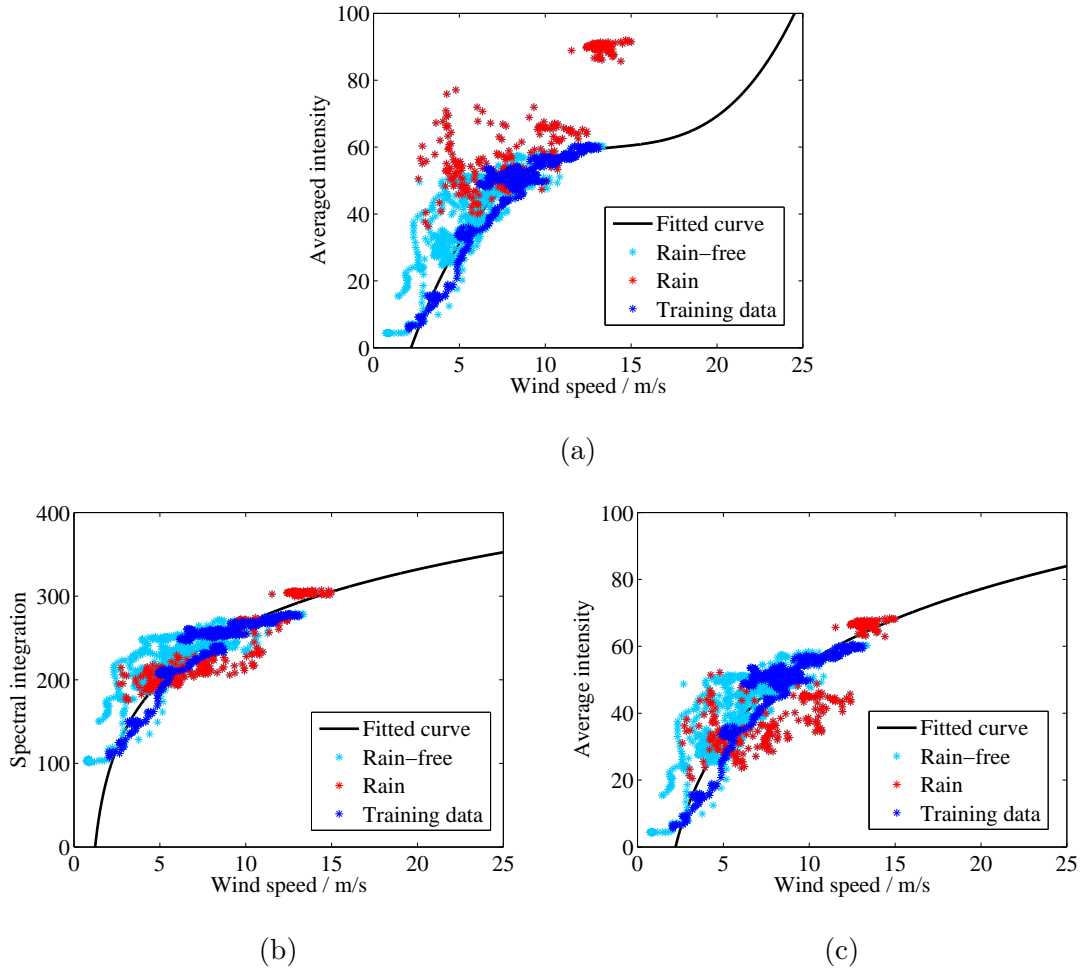
Figure 3.8: (a) Scatter plot showing the anemometer wind speed, the corresponding radar backscatter intensity, and the best-fit third-order polynomial based on the curve fitting method in [21]; (b) scatter plot showing the anemometer wind speed, the corresponding spectral integration of image intensity, and the best-fit logarithmic function based on the proposed method in Section 3.2; (c) scatter plot showing the anemometer wind speed, the corresponding radar backscatter intensity (with gamma correction on rain-contaminated cases), and the best-fit logarithmic function based on the proposed method in Section 3.3.

41
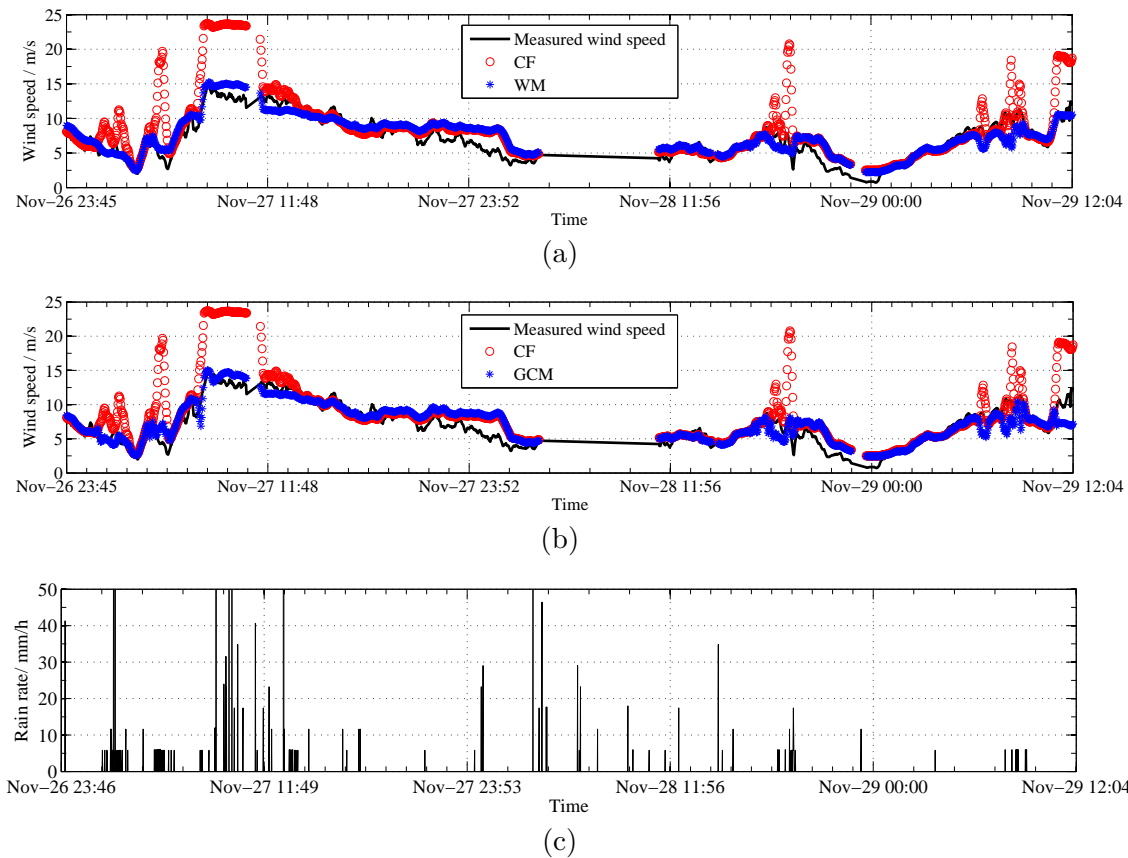
Figure 3.9: Results: (a) Wind speeds results using the curve fitting method in [21] (CF) and the wavenumber-domain-based method in Section 3.2 (WM); (b) wind speeds results using the curve fitting method in [21] (CF) and the gamma correction method in Section 3.3 (GCM); (c) measured rain rates.

Table 3.2: Wind Speed Retrieval Error Statistics: RMSEs

Methods/ Data type	Rain-contaminated Data	Rain-free Data
Curve Fitting Method in [21]	7.5 m/s	1.5 m/s
Wavenumber-domain-based Method	1.6 m/s	1.6 m/s
Gamma Correction Method	2.1 m/s	1.5 m/s

42
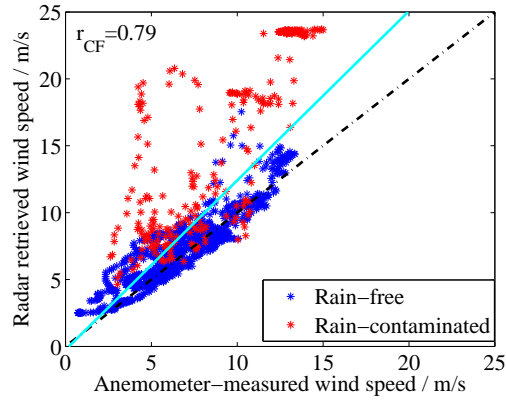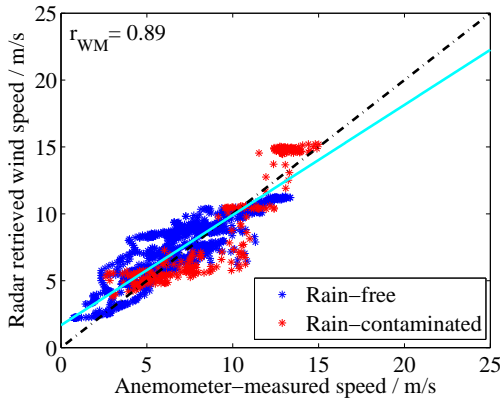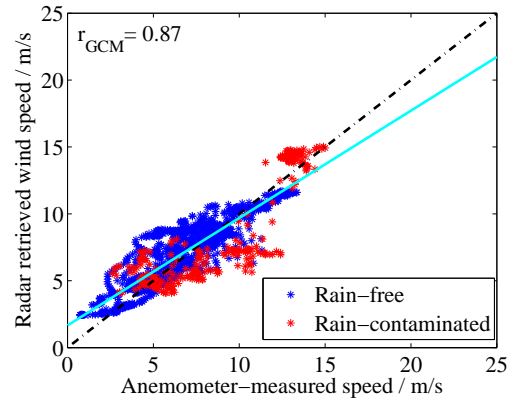
Figure 3.10: (a) Scatter plot of wind speed measured by anemometer and estimates obtained from radar images based on the curve fitting based method in [21] (CF); (b) scatter plot of wind speed measured by anemometer and estimates obtained from radar images based on the wavenumber-domain-based method (WM); (c) scatter plot of wind speed measured by anemometer and estimates obtained from radar images based on the gamma correction method (GCM).

correction method are 7.5 m/s, 1.6 m/s and 2.1 m/s, respectively. The wind speed retrieval accuracy for rain-contaminated images has been improved by 5.9 m/s with the wavenumber-domain-based method, 5.4 m/s with the gamma correction method. For the rain-free images used for validation, the RMSEs of wind speeds retrieved using the curve fitting method in [21], the wavenumber-domain-based method and the gamma correction method are 1.5 m/s, 1.6 m/s and 1.5 m/s, respectively. The performance of the proposed two methods is almost the same as that of the curve fitting method in [21] under rain-free conditions. The scatter plots of the anemometer data and radar results obtained using the curve fitting method in [21] and the proposed two methods are shown in Fig. 3.10 (a), (b) and (c), respectively. From Fig. 3.10, it can be seen that the correlation coefficient between the radar-derived and the anemometer-measured wind speeds is improved by 0.1 and 0.08 using the proposed methods.

It should be noted that rain-contaminated data were not included in training the relationship between radar measurements and reference wind speeds. This has been done to ensure that the training and validating data sets for all the three methods were exactly the same, since the training process of the curve fitting method in [21] requires the elimination of rain-contaminated data. However, it was found that rain-contaminated data could be included for training in the proposed two methods without decreasing the performance.
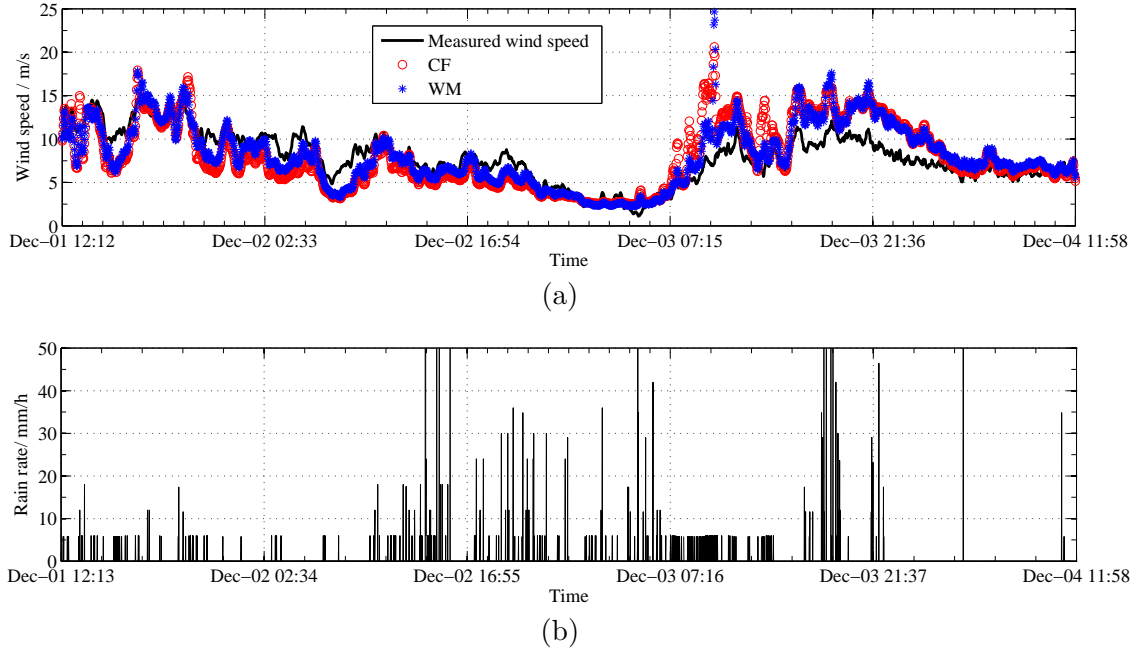
Figure 3.11: Results: (a) retrieved wind speeds for data in Furuno dataset using the curve fitting based method in [21] (CF) and the wavenumber-domain-based method (WM); (b) measured rain rates for the Furuno dataset.

3.5.2 Wind Speed Retrieval Results of Furuno Dataset

The wavenumber-domain-based method and the curve fitting based method were applied to the Furuno dataset. As shown in Section 3.4.1, images in the Furuno dataset were pre-filtered. Thus, the traditional image classification method cannot correctly identify all rain-contaminated images. That's why the gamma correction method as well as the wind direction retrieval method introduced in Section 2.2 were not applied to the Furuno dataset. The wavenumber-domain-based wind speed retrieval method does not require the separation of rain-contaminated images from rain-free images. Thus, it was also applied to the Furuno dataset to test whether it can be used to improve wind speed retrieval accuracy for pre-filtered images. The retrieved wind

45

speeds using the curve-fitting-based method in [21] and the wavenumber-domain-based method are averaged over a ten-minute sliding window and shown in Fig. 3.11 (a). The rain rates obtained from the rain gauge are shown in Fig. 3.11 (b). For all images in this dataset, the RMSEs of retrieved wind speeds using the curve-fitting-based method in [21] and the proposed wavenumber-domain-based method are 2.9 m/s and 2.4 m/s. The proposed wavenumber-domain-based method improved the overall wind speed retrieval accuracy by 0.5 m/s for the Furuno dataset. However, the improvement is not large compared with that for the Decca dataset.

3.6   Chapter Summary

Two methods, the wavenumber-domain-based method and the gamma correction method, for determining wind speeds from X-band nautical radar images have been proposed. The methods can be applied to both rain-contaminated and rain-free images. Comparison with the curve fitting method in [21] based on the Decca dataset shows that the wind speed retrieval accuracy from rain-contaminated images has been improved by 5.9 m/s using the proposed wavenumber-domain-based method, and 5.4 m/s using the proposed gamma correction method. The correlation coefficient for the wind speeds retrieved from radar data and measured by anemometers has been increased by 0.1 and 0.08 using the proposed wavenumber-domain-based method and the gamma correction method, respectively.

The wind speed results from the Furuno dataset show that the improvement of the proposed wavenumber-domain-based method on pre-filtered data is limited. Thus, non-pre-filtered radar data are suggested before applying the proposed two methods.

Chapter 4

Conclusions

4.1 General Synopsis and Significant Results

In this thesis, research for wind information retrieval from X-band marine radar data has been presented. Firstly, a wavenumber-domain-based method for wind direction retrieval from both rain-contaminated and rain-free marine radar images was presented. Secondly, two methods for improving wind speed retrieval accuracy from rain-contaminated data were proposed. The first approach was developed based on the analysis in the wavenumber domain. The second approach was designed by mitigating the effects of rain with a gamma correction in the space domain.

The main contribution of the proposed wind direction retrieval method is that it allows wind direction to be retrieved from rain-contaminated images. Unlike traditional methods [20,21,43], which use intensity information only, the proposed method employs both intensity and intensity variation information. This is achieved by applying a one-dimensional Fourier Transform to radar backscatter in each azimuth

direction. An advantage of the proposed method is that it has a good compatibility with the traditional curve-fitting-based method in [21]. As shown in Chapter 2, intensity information could be well represented by the zero wavenumber component of the wavenumber spectra. By selecting the zero wavenumber component under rain-free conditions, the proposed method can be used to obtain exactly the same results as the curve-fitting-based method in [21].

The proposed wind direction retrieval algorithm was applied to 48,004 radar images in the Decca dataset. The results show that the wind direction retrieval accuracy for rain-contaminated data has been improved by 25.1° using the proposed method. As for rain-free data, the proposed method maintains the same accuracy as the curve-fitting-based method in [21].

In addition, the wavenumber domain analysis has been extended to improve wind speed retrieval accuracy for rain-contaminated radar images. This forms the first wind speed retrieval method in this thesis. An advantage of this method is that it can be directly applied to radar images, without classifying them as being rain-contaminated or rain-free. The reason for this is that the method takes all spectral components into consideration, including the components associated with intensity variation, which have been ignored in previous methods. Another advantage of this method is its stability. Unlike traditional methods which utilize third-order polynomials to relate the radar backscatter to the measured wind speeds, the proposed method employs a logarithmic function. The advantage of the logarithmic model is that it is a monotonically increasing function and will not decrease under high wind speeds. Moreover, both rain-contaminated and rain-free data may be used in training the proposed algorithm.

The second wind speed retrieval method is performed in the spatial domain. The main contribution of this method is that it can mitigate the nonlinear rain effects to some extent. By applying the gamma correction to rain-contaminated images, both the uniform rain scatter (low-wind-speed rain cases) and the non-uniform rain-induced noise (high-wind-speed rain cases) are reduced. The logarithmic function is also employed in this method.

The two proposed wind speed retrieval methods were applied to 48,004 radar images in the Decca dataset. Compared with curve-fitting-based method in [21], these two methods improve wind speed retrieval accuracy from rain-contaminated cases by 5.9 m/s and 5.4 m/s, respectively. Moreover, it is suggested that the proposed methods should be applied to non-pre-filtered radar images.

4.2   Suggestions for Future Work

It has been noted that the images utilized in Decca dataset are neither pre-filtered nor pre-thresholded. Such images are suggested to be used for retrieving sea surface wind information since they contain more detail of radar backscatter from sea surface. For wind direction retrieval, the proposed method works for 97.4% of the rain-contaminated images. However, the results of the remaining 2.6% are not very good. These images may be partly contaminated by rain with rain appearing in up-wind directions only, or they may contain no wave pattern because the rain is too heavy. More experiments and investigations are needed for these images.

This study employed the gamma correction to mitigate rain effects and to improve wind speed retrieval accuracy. However, the application of the gamma correction may

49

not be limited to wind information only. For example, it also been known that sea surface wave information retrieval is negatively influenced by rain. It may be possible to improve wave information retrieval accuracy using gamma-corrected images. It is expected that the such investigations may provide a better understanding of rain-contaminated X-band marine radar images.

Bibliography

[1] G. R. Valenzuela, "Theories for the interaction of electromagnetic and oceanic waves - A review," *Bound- Lay. Meteorol*, vol. 13(1-4), pp. 61-85, 1978.

[2] H. Oudshoorn, "The use of radar in hydrodynamic surveying,"in *Proc. 7th Coastal Eng.*, Berkeley, California, vol. 1, pp. 59-76, 1960.

[3] M. G. Mattie and D. L. Harris, "A system for using radar to record wave direction," *Techn. 79-1, US Army Corps of Eng., Coastal Engineering Res. Ctr.*, Fort Belvair, 1979.

[4] F. J. Wylie, "The use of radar at sea," *American Elsevier Publishing Company*, 1968.

[5] D. Hasselmann, M. Dunckel, and J. Ewing, "Directional wave spectra observed during jonswap 1973," *J. Phys. Oceanogr.*, vol. 10, no. 8, pp. 1264-1280, 1980.

[6] V. Atanassov, W. Rosenthal, and F. Ziemer, "Removal of ambiguity of two-dimensional power spectra obtained by processing ship radar images of ocean waves," *J. Geophys. Res.*, vol. 90, no. C1, pp. 1061-1067, 1985.

[7] I. R. Young, W. Rosenthal, and F. Ziemer, "A three-dimensional analysis of marine radar images for the determination of ocean wave directionality and surface currents," *J. Geophys. Res.*, vol. 90, no. C1, pp. 1049-1059, 1985.

[8] J. Trask, M. Henschel, and B. Eid, "Analysis of marine radar image spectra collected during the grand banks ers-1 sar wave experiment," *Atmosphere- Ocean*, vol. 32, no. 1, pp. 215-236, 1994.

[9] H. Leung, "Applying chaos to radar detection in an ocean environment: an experimental study," *IEEE J. Ocean. Eng.*, vol. 20, no. 1, pp. 56-64, 1995.

[10] G. Geernaert, K. Davidson, S. Larsen, and T. Mikkelsen, "Wind stress measurements during the tower ocean wave and radar dependence experiment," *J. Geophys. Res.*, vol. 93, no. C11, pp. 13913-13923, 1988.

[11] C. Gommenginger, N. Ward, G. Fisher, I. Robinson, and S. Boxall, "Quantitative microwave backscatter measurements from the ocean surface using digital marine radar images," *J. Atmos. Ocean. Tech.*, vol. 17, no. 5, pp. 665-678, 2000.

[12] J. Nieto Borge, G. R. RodrÍguez, K. Hessner, and P. I. González, "Inversion of marine radar images for surface wave analysis," *J. Atmos. Ocean. Technol.*, vol. 21, no. 8, pp. 1291-1300, 2004.

[13] R. Bürgmann, P. A. Rosen, and E. J. Fielding, "Synthetic aperture radar interferometry to measure earth's surface topography and its deformation," *Ann. Rev. Earth. Planet. Sci.*, vol. 28, no. 1, pp. 169-209, 2000.

[14] J. D. Paduan and L. K. Rosenfeld, "Remotely sensed surface currents in monterey bay from shore-based HF radar (coastal ocean dynamics application radar)," *J. Geophys. Res.*, vol. 101, pp. 20-669, 1996.

[15] X. Liu, W. Huang, and E. W. Gill, "Wave height estimation from shipborne X-band nautical radar images," *J. Sensors*, vol. 501, pp. 376-309, 2015.

[16] P. H. Y. Lee, J. D. Barter, K. L. Beach, C. L. Hindman, B. M. Lake, H. Rungaldier, J. C. Shelton, A. B. Williams, R. Yee, and H. C. Yuen, "X-band microwave backscattering from ocean waves," *J. Geophys. Res.*, vol. 100, no. C2, pp. 2591-2611, Feb. 1995.

[17] D. Trizna, "A model for Brewster angle effects on sea surface illumination for sea scatter studies," *IEEE Trans. Geosci. Remote Sens.*, vol. 35, no. 5, pp. 1232-1244, 1997.

[18] H. Hatten, F. Ziemer, J. Seemann, and J. Nieto-Borge, "Correlation between the spectral background noise of a nautical radar and the wind vector," in *Proc. 17th OMAE Conf.*, OMAE98-4451, Lisbon, Portugal, 1998.

[19] H. Dankert, J. Horstmann, and W. Rosenthal, "Ocean wind fields retrieved from radar-image sequences," *J. Geophys. Res.: Oceans*, vol. 108, no. C11, pp. 16-1-16-11, Nov. 2003.

[20] H. Dankert and J. Horstmann, "A marine radar wind sensor," *J. Atmos. Ocean. Technol.*, vol. 24, no. 9, pp. 1629-1642, Sep. 2007.

[21] B. Lund, H. C. Graber, and R. Romeiser, "Wind retrieval from shipborne nautical X-band radar data," *IEEE Trans. Geosci. Remote Sens.*, vol. 50, no. 10, pp. 3800-3811, Oct. 2012.

[22] W. Bragg and W. Bragg, "The refection of x-rays by crystals," in *Proc. Royal Soc.*, Series A, pp. 428-438, 1913.

[23] J. W. Wright, "Backscattering from capillary waves with application to sea clutter," *IEEE Trans. Antennas Propag.*, vol. 14, no. 6, pp. 749-754, 1966.

[24] J. W. Wright, "A new model for sea clutter," *IEEE Trans. Antennas Propag.*, vol. 16, no. 2, pp. 217-223, Mar. 1968.

[25] F. G. Bass, and A. Kalmykov, "Very high frequency radiowave scattering by a disturbed sea surface Part I: Scattering from a slightly disturbed boundary," *IEEE Trans. Antennas Propag.*, vol. 16, no. 5, pp. 554-559, 1968.

[26] S. T. Wu, and A. K. Fung, "A noncoherent model for microwave emissions and backscattering from the sea surface," *University of Kansas Center for Research, National Aeronautics and Space Administration, NASA Contractor Report*, vol. 2326, 1973.

[27] M. W. Long, "On a two-scatterer theory of sea echo, " *IEEE Trans. Antennas Propag.*, vol. 22, no. 5, pp. 667-672, 1974.

[28] H. L. Chan, and A. K. Fung, "A theory of sea scatter at large incident angles," *J. Geophys. Res.*, vol. 82, no.24, pp. 3439-3444, 1977.

[29] A. I. Kalmykov and V. V. Pustovoytenko, "On polarization features of radio signals scattered from the sea surface at small grazing angles," *J. Geophys. Res.*, vol. 81, no. 12, pp. 1960-1964, Apr. 1976.

[30] D. R. Lyzenga, A. L. Maffett, and R. A. Shuchman, "The contribution of wedge scattering to the radar cross section of the ocean surface," *IEEE Trans. Geosci. Remote Sens.*, vol. 21, no. 4, pp. 502-505, Oct. 1983.

[31] W. K. Melville, "The role of surface-wave breaking in air-sea interaction," *Annu. Rev. Fluid. Mech.*, vol. 28, no.1, pp. 279-321, 1996.

[32] M. L. Banner, "The influence of wave breaking on the surface pressure distribution in wind-wave interactions," *J. Fluid Mech.*, vol. 211, pp. 463-495, 1990.

[33] S. Carniel, J. C. Warner, J. Chiggiato, and M. Sclavo, "Investigating the impact of surface wave breaking on modeling the trajectories of drifters in the northern adriatic sea during a wind-storm event," *Ocean Modelling*, vol. 30, no. 2, pp. 225-239, 2009.

[34] L. B. Wetzel, "Electromagnetic scattering from the sea at low grazing angles," *Surface Waves and Fluxes*, vol. 2, pp. 109-171, 1990.

[35] W. J. Plant, and W. C. Keller, "Evidence of Bragg scattering in microwave Doppler spectra of sea return," *J Geophys. Res.: Oceans*, vol. 95, no. C9, pp. 16299-16310, 1990.

[36] W. J. Plant, "Microwave sea return at moderate to high incidence angles," *Wave. Random Media*, vol. 13, no. 4, pp. 339-354, Jul. 2003.

[37] P. Hoogeboom, and W. Rosenthal, "Directional wave spectra in radar images, " in *Int. Geosci. and Remote Sens. Symp., IEEE Geosci. and Remote Sens. Soc.,* Munich, June 1982.

[38] F. Ziemer, W. Rosenthal, and H. Carlson, "Measurements of directional wave spectra by ship radar," *IAPSO Symp., General Assembly, Int. Assoc. Phys. Sci. Oceans,* Hamburg, 1983.

[39] P. W. Vachon, and F. W. Dobson, "Validation of wind vector retrieval from ERS-1 SAR images over the ocean," *Global Atmos. Ocean Syst.,* vol. 5, no. 2, pp. 177-187, 1996.

[40] E. Korsbakken, J. A. Johannessen, and O. M. Johannessen, "Coastal wind field retrievals from ERS synthetic aperture radar images," *J. Geophys. Res.: Oceans,* vol. 103, no. C4, pp. 7857-7874, 1998.

[41] D. B. Trizna and D. J. Carlson, "Studies of dual polarized low grazing angle radar sea scatter in nearshore regions," *IEEE Trans. Geosci. Remote Sens.,* vol. 34, no. 3, pp. 747-757, May 1996.

[42] H. Hatten, J. Seemann, J. Horstmann, and F. Ziemer, "Azimuthal dependence of the radar cross section and the spectral background noise of a nautical radar at grazing incidence," in *Proc. Geosic. Remote Sens. Symp,* vol. 5, pp. 2490-2492, 1998.

[43] R. Vicen-Bueno, J. Horstmann, E. Terril, T. De Paolo, and J. Dannenberg, "Real-time ocean wind vector retrieval from marine radar image sequences ac-

quired at grazing angles," *J. Atmos. Ocean. Technol.*, vol. 30, no. 1, pp. 127-139, Jan. 2013.

[44] Y. Liu, W. Huang, and E. W. Gill, "Analysis of the effects of rain on surface wind retrieval from X-band marine radar images," in *Proc. MTS/IEEE Oceans' 14*, St. John' s, Canada, 2014.

[45] C. Craeye, P. W. Sobieski, L. F. Bliven, and A. Guissard, "Ring-waves generated by water drops impacting on water surfaces at rest," *IEEE J. Ocean. Eng.*, vol. 24, no. 3, pp. 323-332, 1999.

[46] N. Braun, M. Gade, and P. A. Lange, "The effect of artificial rain on wave spectra and multi-polarisation X band radar backscatter," *Int. J. Remote Sens.*, vol. 23, no. 20, pp. 4305-4323, 2002.

[47] M. Tsimplis and S. A. Thorpe, "Wave damping by rain," *Nature*, vol. 342, no. 6252, pp. 893-895, Dec. 1989.

[48] M. N. Tsimplis, "The effect of rain in calming the sea," *J. Phys. Oceanogr.*, vol. 22, no. 4, pp. 404-412, Apr. 1992.

[49] Z. Yang, S. Tang and J. Wu, "An experimental study of rain effects on fine structures of wind waves," *J. Phys. Oceanogr.*, vol. 27, no. 3, pp. 419-130, 1997.

[50] R. K. Moore, Y. S. Yu, A. K. Fung, D. Kaneko, G. J. Dome, and R. E. Werp, "Preliminary study of rain effects on radar scattering from water surfaces," *IEEE J. Oceanic Eng.*, vol. oe-4, no.1, pp. 31-32, Jan. 1979.

[51] Y. K. Poon, S. Tang, and J. Wu, "Interactions between rain and wind waves," *J. Phys. oceanogr.*, vol. 22, no. 9, pp. 976-987, 1992.

[52] N. Braun, M. Gade, and P. Lange, "Radar backscattering measurements of artificial rain impinging on a water surface at different wind speeds," in *Proc of IEEE Geosci. and Remote Sens. Symp.*, vol. 1, 1999.

[53] D. E. Weissman, M. A. Bourassa, and J. Tongue, "Effects of rain rate and wind magnitude on SeaWinds scatterometer wind speed errors," *J. of Atmos. Ocean. Technol.*, vol. 19, no. 5, pp. 738-746, 2002.

[54] R. F. Contreras and W. J. Plant, "Surface effect of rain on microwave backscatter from the ocean: measurements and modelling," *J. Geophys. Res.*, vol. 111, no. C8, C08019, Aug. 2006.

[55] W. Huang and E. W. Gill, "Ocean remote sensing using X-band shipborne nautical radar - applications in eastern Canada," in *Coastal Ocean Observing Systems: Advances and Syntheses*, 1st ed., London, UK: Academic Press, 2015, Ch. 15, pp. 248-264.

[56] C. A. Poynton, "Gamma," in *Digital Video and HDTV: Algorithms and Interfaces*, Amsterdam, Netherlands: Morgan Kaufmann Publishers, 2003, ch. 23, pp. 258-279.

[57] Y. Wang and W. Huang, "An algorithm for wind direction retrieval from X-band marine radar images," *IEEE Geosci. Remote Sens. Lett.*, vol. 13, no. 2, pp. 252-256, 2016.

[58] Y. Wang and W. Huang, "Wind direction retrieval from rain-contaminated X-band nautical radar images," in *Proc. MTS/IEEE Oceans' 15*, Washington DC, USA, Oct. 2015.

[59] B. Lund, H. Graber, R. Romeiser, H. Tamura, J. Xue, T. Collins, J. Horstmann, R. Carrasco, C. Lido, E. Terrill, E. Shroyer, and J. Moum, "Marine radar surface wave, internal wave, and wind retrieval- with a focus on shipborne data," presented at the *Second Workshop on Sensing the Ocean with Marine Radar*, Lerici, Italy, June 2013.

[60] (2012, May). WaMoS II Wave and surface current monitoring system operating manual version 4.0. [Online]. Available: oceanwaves.org.

[61] Y. Liu, W. Huang, E. W. Gill, D. K. Peters, and R. Vicen-Bueno, "Comparison of algorithms for wind parameters extraction from shipborne X-band marine radar images," *IEEE J. Sel. Topics Appl. Earth Observ. Remote Sens.*, vol. 8, no. 2, pp. 896-906, Sep. 2014.

[62] W. Huang and Y. Wang, "A spectra-analysis-based algorithm for wind speed estimation from X-band nautical radar images," *IEEE Geosci. Remote Sens. Lett.*, vol. 13, no. 5, 2016. (In press, DOI: 10.1109/JOE.2015.2505778)

[63] N. W. Guinard, J. T. Ransone, and J. C. Daley, "Variation of the NRCS of the sea with increasing roughness," *J. Geophys. Res.*, vol. 76, no. 6, pp. 1525-1538, 1972.

[64] M. W. Long, R. D. Wetherington, J. L. Edwards and A. B. Abeling, "Wavelength dependence of sea echo," Georgia Institute of Technology, Final Report, Project A-840, Contract N622693019, July, 1965.

[65] J. G. Boring, E. R. Flynt, M. W. Long, V. R. Widerquist, "Sea return study," Georgia Institute of Technology, Final Report on Contract NObsr-49063, 1957.

[66] R. H. Wanninkhof and L. F. Bliven, "Relationship between gas exchange, wind speed, and radar backscatter in a large wind-wave tank," *J. Geophys. Res.*, vol. 96, no. C2, pp. 2785-2796, 1991.

[67] S. Soisuvarn, Z. Jelenak, P. S. Chang, S. O. Alsweiss and Q. Zhu, "CMOD5.H- A high wind geophysical model function for C-band vertically polarized satellite scatterometer measurements," *IEEE Trans. Geosci. Remote Sens.*, vol. 51, no. 6, pp. 3744-3760, 2013.

[68] Y. Wang and W. Huang, "Wind speed extraction from rain-contaminated X- band nautical radar data," in *Proc. MTS/IEEE Oceans' 16*, Shanghai, China, 2016.